Hydroelastic analysis of Very Large Floating Structures in variable bathymetry regions by multi-modal expansions and FEM

Angeliki E. Karperaki[(*)] and Kostas A. Belibassakis

School of Naval Architecture and Marine Engineering

National Technical University of Athens, Zografos 15773, Athens, Greece

[(*)]Corresponding author email: akarperaki@mail.ntua.gr

Abstract

A novel frequency domain numerical method for Very Large Floating Structure (VLFS) hydroelasticity is developed. The problem is formulated in the 2D ocean waveguide, featuring a realistic seabed bathymetry and the presence of inhomogeneous, elastic plates of varying thickness and negligible draft. An *in vacuo* modal expansion for the plate deflection is employed to decouple the hydrodynamics from structural mechanics. The inhomogeneous plate is considered to undergo cylindrical bending, while depending on the slenderness and the excited wavelength the structure can be modelled using either Classical Thin Plate theory or Mindlin's model, accounting for first order shear deformation effects. A weighted residual approach is employed to treat the component hydrodynamic problems, coupled with an enhanced vertical representation for the wave potential, able to accurately account for abrupt bathymetric changes, following Athanassoulis and Belibassakis (1999). The reduced weak problem is solved by means of the Finite Element Method (FEM). Finally, a series of comparisons are carried out against published results for a range of configurations.

Keywords: hydroelasticity, variable bathymetry, coupled-mode system, Finite Element Method, Mindlin Plate, VLFS

1   Introduction

Ocean wave interaction with flexible structures finds numerous applications in marine science and technology as well as in ocean and polar engineering. The adjacent fields focus on the study of wave-structure-seabed interaction, targeting engineering structures and geophysical formations, such ice shelves or ice floes, respectively (Squire, 2008). Very Large Floating Structures and floating ice formations share two distinct hydrodynamic features; their large dimensions compared to the incident wavelengths and their bending rigidity which renders flexural modes dominant. Wave-induced structural response and its underlying effect on the hydrodynamic field is important for the in-depth understanding of physical processes like ice shelf calving events (Ilyas et al., 2018; Papathanasiou et al., 2019; Papathanasiou and Belibassakis, 2018; Porter, 2019) and the robust design of engineering structures operating nearshore (Karperaki et al., 2016; Nguyen et al., 2019).

For the treatment of the linearised hydroelastic problem, potential theory is employed for the hydrodynamic modelling. The small wave amplitude assumption, leading to the exclusion of nonlinear and viscous effects is justified by the slenderness of the structure. Considering the above kinematic considerations, the Classical Thin Plate (Kirchhoff-Love) theory is commonly employed for the dynamic response of the floating body (Faltinsen, 2015; Wang et al., 2006; Watanabe et al., 2004).

The linearized problem is effectively treated in the frequency domain with the majority of published works employing a modal expansion technique, aiming at the decoupling of the structural response and the hydrodynamics or proposing a direct solution of the coupled equations (Watanabe et al., 2004). In modal expansion techniques, the structural oscillation is expressed as a series expansion involving a class of basis functions. By means of the underlying linearity assumption, the problem is decomposed into component diffraction and a series of radiation problems corresponding to structural oscillations (Newman, 1994; Taylor and Waite, 1978). For the modal expansion, the 'dry' *in vacuo* modes of the freely floating structure constitute a natural and common choice (Kashiwagi, 1998; Wu et al., 1995). The hydrodynamics and the structural response are fully decoupled allowing for the adoption of different analytical or numerical tools, facilitating the emergence of many computational schemes in the frequency domain (see Squire (2008) and Wang et al. (2006) for a literature review). Subsequently, the motion equation of the plate is satisfied and the dynamic coupling of the wave-field and structure is completed.

While in the majority of published works on hydroelasticity, the structure is modelled as a thin plate, attempts have been made to account for the rotary inertia and shear deformation effects of a plate structure under wave forcing by means of Mindlin, shear deformable plate theory, e.g. Fox and Squire, (1991), Zhao et al. (2008), Praveen et al. (2019). Recently, Praveen and Karmakar (2019) considered the hydroelastic behaviour of a floating Mindlin plate over variable bathymetry. In the latter work, seabed variations are restricted in the hydroeastic region of the 2D fluid strip. Considering general bathymetries, Kyoung et al. (2005) employed a modal expansion h in terms of the *in vacuo* bending modes in conjunction with FEM in the fluid region for the solution of the hydroelastic problem, featuring a homogeneous, rectangular Kirchhoff plate. In the above, the bottom boundary condition is explicitly satisfied. In Liu et al. (2020), the variable bathymetry is approximated by a series of flat steps while local, multi-mode vertical eigenfunction expansions are employed for the representation of the wave potential. Belibassakis and Athanassoulis (2005) proposed a continuous coupled-mode technique for the hydroelastic analysis of a uniform thin, semi-infinite plate of shallow draft, floating over variable bathymetry regions. The bottom boundary condition in the non-separable domain is consistently satisfied by means of the additional sloping bottom mode. A highly desirable feature of the above work is that it leads to dimensionality reduction with no underlying assumptions with respect to the bottom slope or curvature. The method was later extended for the treatment of the full 3D bathymetric effects and finite rectangular plates in Gerostathis et al. (2016). In a related note, single-mode and multi-mode vertical expansions were also employed by Porter and Porter (2004) and Bennetts et al. (2007) respectively in the 2D scattering problem by a thin plate of variable thickness. In the aforementioned works accounting for non-negligible draft, a variational principle is appropriately augmented by an auxiliary functional featuring a Lagrange multiplier function in order to weakly satisfy continuity conditions across the fluid-structure interface. In the present contribution, a weighted residuals approach is adopted instead of a variational principle. A Lagrange multiplier formulation of the weak problem is subsequently employed for the satisfaction of the essential condition for the velocity potential, implying continuity, across the fictitious interfaces between free-surface and plate-covered subregions.

More specifically, in the present work a novel frequency domain method for the treatment of the hydroelastic problem, able to account for shear deformation effects, structural inhomogeneity and variable bathymetry is presented. In order to decouple the hydrodynamic analysis and the structural dynamics analysis, modal expansion for the plate deflection in terms of its *in vacuo* free bending modes, is employed. The latter leads to the decomposition of the problem to its diffraction and radiation components. Within the scope of this work, the structural response is modelled by the Kirchhoff-Love thin plate theory and Mindlin's theory for thicker plates.

After the formulation of the hydroelastic problem in Section 2, the work focuses on the treatment of the diffraction and radiation subproblems, as well as the composition of the final solution. The incident to the structure wavefield, propagating in the inhomogeneous waveguide is calculated by means of the consistent

coupled-mode system proposed in Athanassoulis and Belibassakis (1999). Subsequently, in Section 3.1, a weighted residuals approach is employed for the unified treatment of the model radiation-type problem, which is recast into a formulation involving Lagrange multiplier functions, employed for the weak satisfaction of the transmission conditions across the fictitious interfaces between free-surface and plate-covered regions. Next, in Section 3.2, the enhanced local-mode representation for the wave potential, originally proposed by Athanassoulis and Belibassakis (1999) is employed for the dimensionality reduction of the model radiation-type problem. The enhanced vertical representation features an additional mode, referred as the sloping bottom mode, accounting for higher order bathymetric slopes. Next, in Section 3.3, the FE method is employed for the discretization of the reduced weak problem involving only the horizontal co-ordinate. In Section 4, Galerkin's method is employed for the satisfaction of the pressure condition on the plate-covered region and the composition of the final solution. Finally, numerical investigations and a range of validation cases are shown in Section 5. The paper concludes with some remarks on the effectiveness of the proposed method and future extensions.

2   Statement of the hydroelastic problem

The hydroelastic interactions between linear water waves and a floating, slender elastic body over a variable bathymetry region is examined in the present section. The considered marine environment consists of a two-dimensional layer $D \subset \mathbb{R}^2$. The flow is assumed irrotational, while Cartesian coordinates (x, z) with z pointing upwards and $z = 0$ coinciding with the mean sea level are employed. The layer is bounded below by an impermeable seabed, located at $z = -h(x)$, $h(x)$ being the smooth depth function. It is also assumed that the free water surface is partially constrained by the presence of a floating elastic structure, modeled as an inhomogeneous plate of shallow draft. Without loss of generality, the introduced inhomogeneity by the variable seabed and the floating body is assumed to be contained in a finite subdomain of the layer, $\Omega(x, z) \subset D$ with smooth boundary $\partial\Omega \equiv \Gamma$. The upper and bottom surface boundaries in Ω are denoted by Γ_f and Γ_b respectively. In the external domain $\Omega^* = \Omega_\infty^- \cup \Omega_\infty^+$, the seabed is assumed to remain constant, albeit at different levels denoted as h^- and h^+ respectively. In essence, the exterior Ω^* is comprised of the positive and negative half-strips. The coincident interface between Ω and Ω^* is denoted as $\Gamma_c = \bigcup_{i=1}^{2} \Gamma_c^{(i)}$. (*see* Fig. 1).
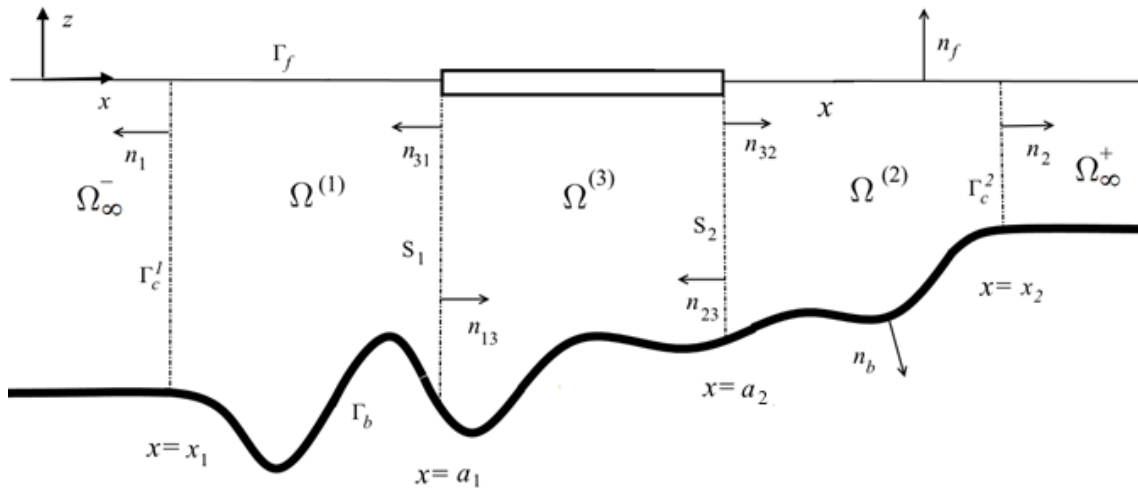
Fig.1. Domain configuration

For the purposes of the present analysis, Ω is assumed to consist of three non-overlapping subdomains $\Omega^{(i)}\,(i=1,2,3)$, with smooth boundaries $\partial\Omega^{(i)}$ such that, $\bigcup\limits_{i=1}^{3}\bar{\Omega}^{(i)}=\bar{\Omega}$ and $\bigcap\limits_{i=1}^{3}\Omega^{(i)}=\varnothing$. The upper and lower boundary of each subdomain consist of their respective restrictions on Γ_f and Γ_b denoted as $\Gamma_f^{(i)}$ and $\Gamma_b^{(i)}$.

Furthermore, the decomposition leads to the creation of the geometrically conforming, internal interfaces $S_{ij}=\partial\Omega^{(i)}\cap\partial\Omega^{(j)}$, as depicted in Fig. 1. The exterior normal vector to a fictitious interface, directed to the exterior of each subdomain is denoted as n_{ij}, while it holds that $n_{ij}=-n_{ji}$. The fictitious interfaces S_{ij} and S_{ji} match, and it is readily reduced that $S_{ij}\equiv S_{ji}=S_i$, for $i=1,2$. Vertical interfaces S_i correspond to the intervals $-h(a_i)<z<0$, located at $x=a_i$, $i=1,2$, respectively.

Under the small wave-amplitude and structural motion assumptions, the time-harmonic fluid motion is described by means of a velocity potential function $\Phi=\mathrm{Re}\left\{-\dfrac{a_0 g}{\omega}\varphi(x,z)\exp(-j\omega t)\right\}$ for a single radian frequency ω dependence, where j is the imaginary unit, g is the acceleration of gravity and a_0 is the wave amplitude. The floating body deflection $W=\mathrm{Re}\{w(x)\exp(-j\omega t)\}$ and free-surface elevation $\mathrm{Re}\{\eta(x)\exp(-j\omega t)\}$ are assumed to coincide. Linearity implies that steady state fluid motion is the superposition of a scattered wave potential φ_S, representing the solution for the case of a body that remains fixed in waves, and a radiation wavefield φ_R generated by the induced flexural response due to the incident wave excitation φ_P (Bishop and Price, 1976; Linton and McIver, 2001; Newman, 1994). Wavefield φ_P corresponds to the propagating solution over the variable bathymetry in absence of the floating body. Furthermore, the scattered potential φ_S is the sum of the incident to the body wavefield φ_P, and the diffracted φ_D expressing the disturbance of φ_P due to the fixed body boundary, hence $\varphi_S=\varphi_P+\varphi_D$.

In order to decouple the floating body response from the fluid flow the following series expansion for the plate deflection, in terms of modal functions $w_\ell(x)$ and complex amplitudes c_ℓ, is considered,

$$w(x)=\sum_{\ell}^{N_f}c_\ell w_\ell(x)\ . \tag{1}$$

In the present work, the structure's 'dry' modes are employed in the above expansion. The basis w_ℓ is *a priori* known as the solution of an *in vacuo* eigenvalue problem for the inhomogeneous structure. A finite number of terms N_f is kept in the truncated infinite series expansion, Eq. (1). The *in vacuo* eigenvalue problem of the inhomogeneous structure is solved by means of the finite element method, as discussed in the sequel.

The radiation potential φ_R is also represented by a series, employing the potential functions φ_ℓ that correspond to unit amplitude fluid motion generated by the ℓth mode w_ℓ. Thus, the total radiation potential is written as,

$$\varphi_R(x,z)=\sum_{\ell=1}^{N_f}c_\ell\varphi_\ell(x,z), \tag{2}$$

while the total normalized potential $\varphi(x,z)$,

$$\varphi(x,z) = \varphi_P(x,z) + \varphi_0(x,z) + \sum_{\ell=1}^{N_f} c_\ell \varphi_\ell(x,z). \tag{3}$$

The treatment of the component radiation problems, denoted as $\varphi_\ell(x,z)$ for $\ell = 1, 2, \ldots$, and the diffraction potential defined in the bounded subdomain Ω, denoted as $\varphi_0(x,z) = \varphi_D(x,z)$, is the focus of the present work. The potential φ_P associated with the incident wavefield, propagating in the inhomogeneous strip, will be considered known and obtained by means of the consistent coupled-mode system proposed by Athanassoulis and Belibassakis (2009). In a unified notation, the radiation-type potentials in the semi-infinite strips $\Omega^\pm$ are written by means of the following representations derived by separation of variables,

$$\varphi_\ell(x,z) = C_0^- \exp(-jk_0^- x)Z_0^-(z) + \sum_{n=1}^{\infty} C_n^- Z_0^-(z)\exp\left(k_n^-(x-x_1)\right)Z_0^-(z), \ (x,z)\in\Omega_\infty^-, \tag{4a}$$

$$\varphi_\ell(x,z) = C_0^+ \exp(jk_0^+ x)Z_0^+(z) + \sum_{n=1}^{\infty} C_n^+ Z_0^+(z)\exp\left(k_n^+(x_2-x)\right)Z_0^+(z), \ (x,z)\in\Omega_\infty^+, \quad \ell = 0,1,2,\ldots \tag{4b}$$

The series expansions Eqs. (4a,b) model outgoing solutions to infinity, where the upscript notation $-,+$ denotes the restriction to the left and right half-strips respectively. The first terms (for $n=0$) in Eqs. (4a,b) correspond to propagating modes, while the remaining terms to evanescent modes. The sets of vertical functions $\{Z_n^\pm, n=0,1,2\ldots\}$ and wavenumbers $\{jk_0^\pm, k_n^\pm, n=1,2\ldots\}$ are the eigenpairs of the vertical Sturm-Liouville problems defined in the constant depth strips Ω_∞^- and Ω_∞^+. The solutions of the regular eigenvalue problems, are,

$$Z_0^\pm = \frac{\cosh\left[k_0^\pm\left(z+h^\pm\right)\right]}{\cos\left(k_0^\pm h^\pm\right)} \ , \quad Z_n^\pm = \frac{\cos\left[k_n^\pm\left(z+h^\pm\right)\right]}{\cos\left(k_n^\pm h^\pm\right)}, n=1,2,\ldots \ , \tag{5}$$

while $\{jk_0^\pm, k_n^\pm\}$ are the roots of the locally defined dispersion relation $\mu h^\pm = -k_n^\pm h^\pm \tan\left(k_n^\pm h^\pm\right)$ for $n=0,1,2,\ldots$. Based on the above, radiation-type problems are formulated in the fluid layer satisfying the following governing equation,

$$\nabla^2 \varphi_\ell = 0, \text{ for } (x,z)\in\Omega, \text{ for } \ell = 0,1,2,\ldots. \tag{6}$$

The combined linearized free-surface condition is satisfied at the free-water surface regions,

$$\partial_z \varphi_\ell - \mu\varphi_\ell = 0, \text{ on } \Gamma_f^{(i)}, \text{ for } i=1,2 \ , \tag{7}$$

where $\mu = \omega^2 g^{-1}$ denotes the frequency parameter. In the plate-covered region the following upper surface kinematic condition is imposed,

$$\partial_z \varphi_\ell + j\omega w_\ell = 0, \text{ on } \partial\Gamma_f^{(3)} \text{ for } \ell = 1,2,\ldots \ , \tag{8a}$$

while for the diffracted potential it holds,

$$\partial_z \varphi_S = 0, \text{ on } \partial \Gamma_f^{(3)} \quad \text{or} \quad \partial_z \varphi_0 = -\partial_z \varphi_P, \text{ on } \partial \Gamma_f^{(3)}. \tag{8b}$$

In a unified formulation the kinematic conditions on $\Gamma_f^{(3)}$ Eqs. (8), for the model diffraction/ ℓ^{th} radiation problem reduce to,

$$\frac{\partial \varphi_\ell}{\partial n} = -V, \text{ on } \Gamma_f^{(3)} \text{ for } \ell = 0, 1, 2, ..., \tag{9}$$

where $V(x) = \dfrac{\partial \varphi_P}{\partial n}$ and $V(x) = i\omega w_\ell$ for the diffraction $(\ell = 0)$, and radiation subproblems respectively $(\ell = 1, 2, ...)$. The kinematic constraint on the impermeable seabed leads to the following condition,

$$\left(\partial_z + \partial_x h \cdot \partial_x \right) \varphi_\ell = 0, \text{ on } \Gamma_b. \tag{10}$$

Finally, matching conditions must hold at the interfaces between the inhomogenous region and the half-strips,

$$\partial_z \varphi_\ell - \mathcal{F}_i[\varphi_\ell] = 0, \text{ on } \Gamma_c^{(i)}, i = 1, 2, \tag{11}$$

where $\mathcal{F}_i$ are appropriate Dirichlet-to-Neumann (DtN) operators ensuring the complete matching between the interior and exterior wavefield solutions on the vertical interfaces $\Gamma_c^{(i)}$ for $i = 1, 2$. The functional form of $\mathcal{F}_i$ is easily computed by means of the series representations, Eqs. (4a,b), valid in the two semi-infinite strips. Equations (11) provide the necessary closure conditions, formulating the radiation-type problem in the truncated region of interest (Belibassakis, 2008). Alternatively, the solvability of the above boundary value problem is ensured by extending the truncation boundaries $\Gamma_c^{(i)}$ within the homogenous strip (at least a distance of the order of one wavelength) and imposing the Sommerfeld radiation conditions,

$$\lim_{x \to \mp\infty} \left(\partial_x \varphi_\ell - jk_0^{(i)} \varphi_\ell \right) = 0, \text{ on } \Gamma_c^{(i)}, i = 1, 2 \tag{12}$$

where $k_0^{(i)}$ are the corresponding wavenumbers associated with the propagating mode at local depth $h^\mp$ at $x = x_1$ and $x = x_2$ accordingly, obtained by means of the dispersion relation $\omega^2 = k_0 g \tanh(kh)$.

Equations (6)–(12) describe the radiation type subproblems defined by the kinematic restrictions imposed on a section of the fluid surface covered by the floating body. Coupling between the total fluid and structural motion is completed by means of the pressure equation on the coupling surface. The following equations of vertical motion involving the unknown deflection $w(x)$ and rotation $\theta(x)$ and total velocity potential on the joint surface,

$$\mathcal{L}_w\{w, \theta\} = -\rho_w g w(x) + j\omega\rho_w \varphi\big|_{z=0}, \tag{13a}$$
$$\mathcal{L}_\theta\{w, \theta\} = 0, \text{ on } \partial\Gamma_f^{(3)}, \tag{13b}$$

where $\mathcal{L}_w, \mathcal{L}_\theta$ are differential operators governing the vertical motion of the body modeled as a plate under cylindrical bending. Equations (13) express equilibrium in terms of the unknowns deflection $w(x)$ and rotation $\theta(x)$, under external generalized forces and rotations respectively. Equation (13a) is the pressure

equation, with the *rhs* term being the fluid pressure exerted on the section of the surface occupied by the elastic body.

For the harmonic flexural motions of a body modelled under the Kirchhoff-Love assumptions it is,

$$\mathcal{L}_w\{w,\theta\} = \mathcal{L}_w\{w\} = \partial_{xx}\left[D(x)\partial_{xx}w(x)\right] - \omega^2 \rho_e \tau(x) w(x),$$
(14a)

$$\mathcal{L}_\theta\{w,\theta\} \equiv \partial_x w(x) - \theta(x) = 0.$$
(14b)

In Eq. (5a), $D(x) = E\tau^3/12(1-v^2)$ denotes the flexural rigidity per unit length in the transverse direction of the plate, ρ_e is the elastic material density, $\tau(x)$ is the plate thickness, E is the Young's modulus and v the Poisson's ratio. It is important to note at this point that the present method is able to account for general inhomogeneity, and thus the spatial variability of material properties, in a straightforward manner. However, the present contribution is limited to the study of variable thickness effects. Kinematic assumptions equate the rotation and slope of the Kirchhoff plate, resulting in a single equation for vertical motion Eq. (12a) under cylindrical bending, rendering Eqs. (13b) and (14b) redundant.

For the modelling of a Mindlin plate accounting for first order shear deformation effects and rotary inertia it holds,

$$\mathcal{L}_w\{w,\theta\} = -\partial_x\left[\kappa G\tau(\partial_x w - \theta)\right] - \omega^2 \rho_e \tau(x) w(x) \quad \text{and}$$
(15a)

$$\mathcal{L}_\theta\{w,\theta\} = -\omega^2 I_r \theta - \kappa G\tau(\partial_x w - \theta) - \partial_x\left[D\partial_x\theta\right].$$
(15b)

In Eqs. (15) $I_r = \rho_e \tau^3/12$ is the rotary inertia per unit length along the transverse dimension of the plate, κ is the shear correction factor and $G = E/2(1+v)$ is the shear modulus. The satisfaction of the dynamic conditions Eqs. (13), supplemented by either Eqs. (13) or (15) by Galerkin's method, will retrieve the complex amplitude functions that will allow the composition of the plate response and the total hydrodynamic solution.

3   Solution of the Diffraction and Radiation Problems

For the domain decomposition formulation of the model diffraction/ ℓ^{th} radiation problem, the solution restriction in each subdomain $\Omega^{(i)}$ is denoted as $\varphi_\ell|_{\Omega^{(i)}} = \varphi^{(i)}$, $i = 1,2,3$, for simplicity. The restriction for the wave potential $\varphi^{(i)}$ refers henceforth to the ℓth radiation-type problem, omitting any subscript for simplicity in presentation. The relevant depth function restriction in each subregion is similarly denoted as $h^{(i)}$. The following tensor product of complex valued spaces is defined,

$$\mathbf{H} = \left\{ \varphi = \left(\varphi^{(1)}, \varphi^{(2)}, \varphi^{(3)}\right) \middle| \varphi^{(i)} \in H^1\left(\Omega^{(i)}; \mathbb{C}\right), i = 1,2,3 \right\}$$

In the analysis the space $H^1\left(\Omega^{(i)}\right)$ denoting the space of square-integrable functions and square-integrable gradient in $\Omega^{(i)}, i = 1,2,3$, trace space $H^{\frac{1}{2}}\left(\partial\Omega^{(i)}\right)$ of H^1 functions as well as the dual space $H^{-\frac{1}{2}}$ are considered (Brezzi and Fortin, 1991). The decomposed problem, Eqs. (6-10) for $\varphi \in \mathbf{H}$, is reformulated as,

$$\nabla^2 \varphi^{(i)} = 0 \text{ , in } \Omega^{(i)}(i = 1,2,3) ,$$
(16a)

$$\text{with } \frac{\partial\varphi^{(i)}}{\partial z} - \mu\varphi^{(i)} = 0 \text{, on } \partial\Gamma_f^{(i)} \text{ for } i = 1,2 \text{ , and } \frac{\partial\varphi^{(3)}}{\partial z} + V = 0 \text{, on } \partial\Gamma_f^{(3)},$$
(16b,c)

7

$$\left(\frac{\partial}{\partial z} + \partial_x h^{(i)} \cdot \partial_x \right) \varphi^{(i)} = 0, \text{ on } \Gamma_b^{(i)} \text{ for } i = 1, 2, 3, \tag{16d}$$

subject to the fictitious interface conditions imposing continuity of momentum and pressure as,

$$\nabla \varphi^{(i)} \cdot \mathbf{n_{i3}} + \nabla \varphi^{(3)} \cdot \mathbf{n_{3i}} = 0, \text{ and } \varphi^{(i)} - \varphi^{(3)} = 0 \text{ on } S_i, \ i = 1, 2 \ . \tag{16e}$$

Closure conditions for the decomposed BVP defined in Ω are provided by imposing the radiation condition, Eq. (12), as discussed above. Hence, at the external, truncated boundary Γ_c it holds,

$$\nabla \varphi^{(i)} \cdot \mathbf{n_i} - j k_0^{(i)} \varphi^{(i)} = 0 \text{ on } \Gamma_c^{(i)}, \text{ for } i = 1, 2. \tag{16f}$$

3.1 Weighted residuals approach

Revisiting the above radiation-type problem, a weighted residuals approach (Finlayson, 2013) is followed in this section. The following function space is defined,

$$\widehat{\mathbf{H}} = \left\{ \left(\varphi^{(1)}, \varphi^{(2)}, \varphi^{(3)} \right) \in \mathbf{H} , \left| \varphi^{(i)} - \varphi^{(3)} = 0 \text{ on } S_i, \ i = 1, 2 \right. \right\}.$$

Following the standard approach, field Eqs. (16a) are multiplied by trial functions $v^{(i)} \in \widehat{\mathbf{H}}$ and integrated over their respective subdomains,

$$\sum_{i=1}^{3} \int_{\Omega^{(i)}} \nabla^2 \varphi^{(i)} \overline{v}^{(i)} \ d\Omega^{(i)} = 0 \ , \tag{17}$$

with the overbar denoting complex conjugation. By means of the Green-Gauss theorem the following expression is derived,

$$-\sum_{i=1}^{3} \int_{\Omega^{(i)}} \nabla \varphi^{(i)} \cdot \nabla \overline{v}^{(i)} \ d\Omega^{(i)} + \sum_{i=1}^{3} \int_{\Gamma_b^{(i)}} \nabla \varphi^{(i)} \cdot \mathbf{n_b} \overline{v}^{(i)} \ ds + \sum_{i=1}^{3} \int_{\Gamma_f^{(i)}} \nabla \varphi^{(i)} \cdot \mathbf{n_f} \overline{v}^{(i)} \ ds$$
$$+ \sum_{i=1}^{2} \int_{S_i} \nabla \varphi^{(i)} \cdot \mathbf{n_{i3}} \overline{v}^{(i)} \ ds + \sum_{i=1}^{2} \int_{S_i} \nabla \varphi^{(i)} \cdot \mathbf{n_{3i}} \overline{v}^{(3)} \ ds + \sum_{i=1}^{2} \int_{\Gamma_c^{(i)}} \nabla \varphi^{(i)} \cdot \mathbf{n_i} \overline{v}^{(i)} ds = 0. \tag{18}$$

Substituting the boundary conditions Eqs. (16b-d) and (16f) results in the following weak formulation of the radiation-type problem,

Find $\varphi^{(i)} \in \widehat{\mathbf{H}}$ such as,

$$\sum_{i=1}^{3} \int_{\Omega^{(i)}} \nabla \varphi^{(i)} \cdot \nabla \overline{v}^{(i)} \ d\Omega^{(i)} - \sum_{i=1}^{2} \int_{\Gamma_f^{(i)}} \mu \varphi^{(i)} \overline{v}^{(i)} \ ds + \int_{\Gamma_f^{(3)}} V \overline{v}^{(i)} \ ds$$
$$+ \sum_{i=1}^{2} \int_{S_i} \left(\overline{v}^{(3)} - \overline{v}^{(i)} \right) \nabla \varphi^{(i)} \cdot \mathbf{n_{i3}} \ ds - \sum_{i=1}^{2} \int_{\Gamma_c^{(i)}} j k_0^{(i)} \varphi^{(i)} \overline{v}^{(i)} \ ds = 0, \quad \forall v^{(i)} \in \widehat{\mathbf{H}}. \tag{19}$$

In the above weak formulation, Eq. (19), essential continuity conditions on the interfaces S_i, are incorporated in the admissible functions space $\widehat{\mathbf{H}}$. To avoid the complexities involved in the construction of appropriate representations for the wave potential functions in $\widehat{\mathbf{H}}$, a Lagrange Multiplier formulation is adopted. Functions $\lambda^{(i)}$ are employed to enable the satisfaction of the continuity requirement in a weak sense across on the interfaces, see (Magoulès and Roux, 2006). Thus Eq. (19) is rewritten,

8

Find $\varphi^{(i)} \in \mathbf{H}$, $\lambda^{(i)} \in H^{-\frac{1}{2}}(S_i)$ such as,

$$\sum_{i=1}^{3} \int_{\Omega^{(i)}} \nabla \varphi^{(i)} \cdot \nabla \overline{v}^{(i)} \, d\Omega^{(i)} - \sum_{i=1}^{2} \int_{\Gamma_f^{(i)}} \mu \varphi^{(i)} \overline{v}^{(i)} \, ds + \int_{\Gamma_f^{(3)}} \overline{v}^{(i)} V \, ds$$

$$- \sum_{i=1}^{2} \int_{S_c^{(i)}} jk_i \varphi^{(i)} \overline{v}^{(i)} \, ds + \sum_{i=1}^{2} \int_{S_i} \lambda^{(i)} \left(\overline{v}^{(3)} - \overline{v}^{(i)} \right) dS = 0, \ \forall v^{(i)} \in \mathbf{H} \quad (20a)$$

$$\int_{S_i} \overline{\xi}^{(i)} \left(\varphi^{(3)} - \varphi^{(i)} \right) dS = 0, \ \forall \xi^{(i)} \in H^{-\frac{1}{2}}(S_i), \ i = 1,2. \quad (20b)$$

From a physical perspective, Lagrange multiplier functions represent potential fluxes on the fictitious interface, i.e. $\lambda^{(i)} = -\nabla \varphi^{(3)} \cdot \mathbf{n_{3i}} = \nabla \varphi^{(i)} \cdot \mathbf{n_{i3}}, i = 1,2$.

3.2   Local-mode representation of the unknown potentials

In this section, a semi-analytical approach will be employed for the approximate solution of Eqs. (20a, b). The unknown velocity potential in each subregion is sought in a separable form, where the vertical structure of the solution, is chosen *a priori*. The approach resembles the Kantorovich method for the dimensionality reduction of boundary value problems, relevant to prismatic domains (Kantorovich and Krylov, 1960). The above technique has been employed for the treatment of linear water wave propagation in variable bathymetry regions by Athanassoulis and Belibassakis (1999) and later extended for wave interaction with thin floating elastic plates (Belibassakis and Athanassoulis, 2005), in conjunction with complete local-mode series expansion of the wave potential involving the local eigenmodes of Laplace equation for the problem under consideration. One advantage of the above choice, is that that the vertical structure of the specific representation is close to the solution of the studied wave problem, as it will be discussed in more detail in the following subsection. Thus, in the scope of the present work the following local-mode series expansion for the unknown wavefields is considered in the free-surface subregions $\Omega^{(i)}$,

$$\varphi^{(i)}(x,z) = \sum_{n=0}^{\infty} \varphi_n^{(i)}(x) \, Z_n^{(i)}(z;x), \quad v^{(i)}(x,z) = \sum_{n=0}^{\infty} v_n^{(i)}(x) \, Z_n^{(i)}(z;x), \quad \text{for } i = 1,2 \ , \quad (21a)$$

while in the plate-covered region $\Omega^{(3)}$ the velocity potential is written as,

$$\varphi^{(3)}(x,z) = \sum_{n=0}^{\infty} \varphi_n^{(3)}(x) \, Y_n(z;x) + \tilde{\varphi}_0(x,z), v^{(3)}(x,z) = \sum_{n=0}^{\infty} v_n^{(3)}(x) \, Y_n(z;x). \quad (21b)$$

It is remarked that the vertical structures employed in the representation of the potential in the free-surface and plate covered subregions (Eqs. 21) are different, and parametrically depended on the horizontal *x*-coordinate. As mentioned above, the coupling between the subdomains is achieved, as previously discussed by means of the introduced Lagrange multiplier functions $\lambda^{(i)}$ that resemble the normal trace of the unknown velocity potential on the interfaces at $x = a_i$, hence   it holds that $\lambda^{(i)}(a_i, z)$. Exploiting the completeness properties of the functions $Z_n(z; x = a_i)$ in the vertical intervals $-h(a_i) < z < 0, i = 1,2,$ in this work the vertical structure of $\lambda^{(i)}(z)$, at $x = a_i$, i=1,2, and their variations $\xi^{(i)}(z)$ are chosen as,

$$\lambda^{(i)}(\alpha_i, z) = \sum_{n=0}^{\infty} \lambda_n^{(i)}(\alpha_i) Z_n^{(i)}(z; \alpha_i), \ i = 1, 2, \quad \xi^{(i)}(\alpha_i, z) = \sum_{n=0}^{\infty} \xi_n^{(i)}(\alpha_i) Z_n^{(i)}(z; \alpha_i), \ i = 1, 2. \quad (22)$$

The vertical functions $Z_n^{(i)}(z; x)$, employed in Eqs. (21a) and (22) are chosen as to explicitly satisfy the boundary conditions on $\Gamma_f^{(i)}$ and $\Gamma_b^{(i)}$ in $\Omega^{(i)}$, $i = 1, 2$. In a similar manner, $Y_n(z; x)$ and $x_0(x, z)$ in Eq (21b) are chosen as to explicitly satisfy the boundary conditions on $\Gamma_f^{(3)}$ and $\Gamma_b^{(3)}$. The choice of the above vertical structures are by no means unique, as long as completeness requirements are satisfied to validate the employment of expansions Eqs (21). However, the performance of the present method heavily relies on the appropriate choice of the above functions.

3.2.1 Vertical expansion for free-surface regions

The functions $Z_n(z; x)$, chosen as the vertical structure of the potential in the free-surface regions are obtained as the solutions of the locally-defined vertical Sturm-Liouville problems at horizontal position x and for every $x \in [x_1, a_1] \cup [a_2, x_2]$. Thus, functions $Z_n(z; x)$ are given as,

$$Z_0 = \frac{\cosh[k_0(x)(z + h(x))]}{\cos(k_0(x)h(x))}, \quad Z_n = \frac{\cos[k_n(x)(z + h(x))]}{\cos(k_n(x)h(x))}, n = 1, 2, \ldots \quad (23a)$$

while $\{jk_0, k_n\}$ are the roots of the locally defined dispersion relation at each horizontal position.

$$\mu h(x) = -k_n(x)h(x)\tan(k_n(x)h(x)), \ x_1 < x < a_1 \text{ and } a_2 < x < x_2. \quad (23b)$$

Revisiting series expansion given in Eq. (21a) in light of Eq. (23a), the first term $\varphi_0 Z_0$ is associated with the propagating mode while remaining terms $\varphi_n Z_n$, for $n = 1, 2, \ldots$, are the evanescent modes in linear water waves. The discrepancy between the above choices of $Z_n(z; x)$, that satisfy $\partial_z Z_n(-h(x); x) = 0$ at the bottom boundary and the kinematic condition on the sloping parts of the seabed, is remedied by the introduction of an additional term for the treatment of the sloping bottom effects, referred as the sloping bottom mode $\varphi_{-1} Z_{-1}$ (Athanassoulis and Belibassakis (1999). The aforementioned, added mode to the classical representation accounts for the incompatibility of the vertical modes of Eq. (23a) with the imposed condition involving the normal derivative of the velocity potential on Γ_b, Eq. (10), and leads to the consistent satisfaction of the kinematic boundary condition on the sloping seabed. The extra horizontal mode, denoted as φ_{-1}, with subscript $n = -1$ acts as a set of additional degrees of freedom that account for the non-homogeneity of the vertical derivative on the seabed. It is evident that the choice for Z_{-1} must lead to solutions that satisfy the upper surface condition Eq. (7) and render φ_{-1} a free variable at the bottom boundary. A convenient, but certainly not unique, choice for the structure of Z_{-1} is,

$$Z_{-1} = h(x)\left[\left(\frac{z}{h(x)}\right)^3 + \left(\frac{z}{h(x)}\right)^2\right] \quad (24)$$

10

The added mode $\varphi_{-1}Z_{-1}$ vanishes at constant depth where $\partial_x h = 0$ retrieving the classical standard representation for the wave potential in the homogeneous strip (Hazard and Lunéville, 2008; Massel, 1993; Porter and Staziker, 1995). Hence, by means of the chosen augmented structure, the expansion of the wave potential in $\Omega^{(i)}$, $i = 1, 2$ involving $N_m + 2$ terms is written,

$$\varphi^{(i)}(x, z) = \sum_{n=-1}^{N_m} \varphi_n^{(i)}(x)Z_n^{(i)}(z; x) = \mathbf{Z}^T \boldsymbol{\varphi}^{(i)}, \quad v^{(i)}(x, z) = \sum_{n=-1}^{N_m} v_n^{(i)}(x)Z_n^{(i)}(z; x) = \mathbf{Z}^T \mathbf{v}^{(i)}, \text{ for } i = 1, 2, \quad (25)$$

where $N_m \in \mathbb{N}$ is the number of evanescent modes in the truncated expansion, which includes the propagating mode $(n = 0)$, and the additional sloping bottom mode, $(n = -1)$. In the above and henceforth, superscript T denotes transposition.

The Lagrange multiplier functions and their variations are written as,

$$\lambda^{(i)}(\alpha_i, z) = \sum_{n=-1}^{N_m} \lambda_n^{(i)}(\alpha_i)Z_n(z; \alpha_i) = \mathbf{Z}^T \boldsymbol{\Lambda}^{(i)} \quad , \xi^{(i)}(\alpha_i, z) = \sum_{n=-1}^{N_m} \xi_n^{(i)}(\alpha_i) \, Z_n^{(i)}(z; \alpha_i) = \mathbf{Z}^T \boldsymbol{\Xi}^{(i)}, \quad i = 1, 2 \quad (26)$$

3.2.2 *Vertical expansions in the hydroelastic region*

The vertical functions $Y_n(z; x)$, employed in Eq. (21b) are obtained as the solutions of the locally-defined vertical Sturm-Liouville problems in $\Omega^{(3)}$ and for every $x \in [a_1, a_2]$:

$$\frac{\partial^2 Y_n(z; x)}{\partial z^2} + \vartheta_n^2(x)Y_n(z; x) = 0, \quad (x, z) \in \Omega^{(3)}, \quad (27a)$$

$$\frac{\partial Y_n(0; x)}{\partial z} = 0, \; z = 0, \qquad\qquad \frac{\partial Y_n(-h; x)}{\partial z} = 0, \; z = -h(x). \quad (27b,c)$$

The eigenvalue problems are again parametrically defined along the horizontal position x, with the solutions are given by

$$Y_n = \cos\left[\vartheta_n(x)z\right], \quad \text{with} \quad \vartheta_n = \frac{n\pi}{h(x)} \text{ for } n = 0, 1, 2, \dots . \quad (28)$$

It is immediately noticed that boundary condition Eq. (27b) is incompatible with kinematic boundary condition Eq. (9). The latter is remedied by the inclusion in Eq. (21b) of an upper surface mode $\tilde{\varphi}_0(x, z) = g(x)f(z; x)$. A judicious choice for the vertical structure of $\tilde{\varphi}_0$ is $f(z; x) = \dfrac{(z + h)^2}{2h}$. Furthermore, setting $g(x) = -V(x)$ allows for the consistent satisfaction of Eq. (9). The sloping bottom mode is also included in the vertical representation of $\varphi^{(3)}$. Finally, keeping the same number of modes N_m in the expansion of $\varphi^{(3)}$ and its variation results in

$$\varphi^{(3)}(x, z) = \sum_{n=-1}^{N_m} \varphi_n^{(3)}(x)Y_n(z; x) + \tilde{\varphi}_0 = \mathbf{Y}^T \boldsymbol{\varphi}^{(3)} + g(x)f(z; x). \quad (29)$$

3.3 Reduced weak form

Substituting Eqs. (26) in Eq. (20a), leaving out the terms involving the Lagrange multipliers to be examined separately, the integral terms corresponding to the free surface regions reduce to,

$$\sum_{i=1}^{2}(-1)^{i+1}\left\{\int_{x_i}^{a_i}\left(\partial_x\overline{\mathbf{v}}^{(i)}\right)^T\mathbb{A}\partial_x\boldsymbol{\varphi}^{(i)}\,dx+\int_{x_i}^{a_i}\left(\overline{\mathbf{v}}^{(i)}\right)^T\mathbb{B}_1\partial_x\boldsymbol{\varphi}^{(i)}dx+\right.$$
$$\left.\int_{x_i}^{a_i}\left(\partial_x\overline{\mathbf{v}}^{(i)}\right)^T\mathbb{B}_2\boldsymbol{\varphi}^{(i)}dx+\int_{x_i}^{a_i}\left(\overline{\mathbf{v}}^{(i)}\right)^T\mathbb{C}\boldsymbol{\varphi}^{(i)}dx\right\}. \tag{30}$$

The above matrix coefficients are defined as,

$$\mathbb{A}=\int_{-h}^{0}\mathbf{Z}\mathbf{Z}^T dz\ ,\ \mathbb{B}_1=\int_{-h}^{0}\mathbf{Z}\left(\partial_x\mathbf{Z}\right)^T dz\ ,\ \mathbb{B}_2=\int_{-h}^{0}\partial_x\mathbf{Z}\mathbf{Z}^T dz\ \text{and}\ \mathbb{C}=\int_{-h}^{0}\left\{\partial_x\mathbf{Z}(\partial_x\mathbf{Z})^T+\partial_z\mathbf{Z}(\partial_z\mathbf{Z})^T\right\}dz-\mu\left[\mathbf{Z}\mathbf{Z}^T\right]_{z=0}.$$

Similarly, for the plate-covered region substituting representations Eq. (29) in Eq. (20a) the corresponding integrals now read,

$$\int_{a_1}^{a_2}\left(\partial_x\overline{\mathbf{v}}^{(3)}\right)^T\tilde{\mathbb{A}}\partial_x\boldsymbol{\varphi}^{(3)}dx+\int_{a_1}^{a_2}\left(\overline{\mathbf{v}}^{(3)}\right)^T\tilde{\mathbb{B}}_1\partial_x\boldsymbol{\varphi}^{(3)}dx+\int_{a_1}^{a_2}\left(\partial_x\overline{\mathbf{v}}^{(3)}\right)^T\tilde{\mathbb{B}}_2\boldsymbol{\varphi}^{(3)}dx$$
$$+\int_{a_1}^{a_2}\left(\overline{\mathbf{v}}^{(3)}\right)^T\tilde{\mathbb{C}}\boldsymbol{\varphi}^{(3)}dx+\int_{a_1}^{a_2}\left\{\left(\partial_x\overline{\mathbf{v}}^{(3)}\right)^T\mathbb{G}_1+\left(\overline{\mathbf{v}}^{(3)}\right)^T\mathbb{G}_2\right\}dx \tag{31}$$

The above matrix coefficients are defined as,

$$\tilde{\mathbb{A}}=\int_{-h}^{0}\mathbf{Y}\mathbf{Y}^T dz\ ,\tilde{\mathbb{B}}_1=\int_{-h}^{0}\mathbf{Y}\left(\partial_x\mathbf{Y}\right)^T dz\ ,\tilde{\mathbb{B}}_2=\int_{-h}^{0}\partial_x\mathbf{Y}\mathbf{Y}^T dz\ \text{ and }\ \tilde{\mathbb{C}}=\int_{-h}^{0}\left\{\partial_x\mathbf{Y}(\partial_x\mathbf{Y})^T+\partial_z\mathbf{Y}(\partial_z\mathbf{Y})^T\right\}dz$$

while the forcing terms as,

$$\mathbb{G}_1=\partial_x\overline{V}\int_{-h}^{0}\left\{f\,\mathbf{Y}\right\}dz+\overline{V}\int_{-h}^{0}\left\{\partial_x f\,\mathbf{Y}\right\}dz\ ,$$

$$\mathbb{G}_2=\partial_x\overline{V}\int_{-h}^{0}f\left(\partial_x\mathbf{Y}\right)\,dz+\overline{V}\int_{-h}^{0}\left(\partial_x f\right)\left(\partial_x\mathbf{Y}\right)dz+\overline{V}\int_{-h}^{0}\left(\partial_z f\right)\left(\partial_z\mathbf{Y}\right)dz+\overline{V}\mathbf{Y}(0)$$

The remaining terms in Eqs. (20) involving the auxiliary functions $\lambda^{(i)}$ and their variations $\xi^{(i)}$ become,

$$\sum_{i=1}^{2}\left\{\left[\left(\mathbf{v}^{(3)}\right)^T\mathbb{P}-\left(\mathbf{v}^{(i)}\right)^T\mathbb{A}\right]\boldsymbol{\Lambda}^{(i)}\right\}_{x=a_i}\ ,\ \text{with}\ \ \mathbb{P}=\int_{-h}^{0}\mathbf{Y}\mathbf{Z}^T dz \tag{32a}$$

$$\text{and}\ \left(\boldsymbol{\Xi}^{(i)}\right)^T\left[\mathbb{P}^T\boldsymbol{\varphi}^{(3)}-\mathbb{A}\,\boldsymbol{\varphi}^{(i)}-\tilde{\mathbb{F}}_i\right]_{x=a_i}=0\ \ ,\ \text{with}\ \ \tilde{\mathbb{F}}_i=\overline{V}(a_i)\int_{-h}^{0}f\mathbf{Z}\,dz\ \text{and}\ i=1,2\ . \tag{32b}$$

The final weak form of the reduced 1-D system of partial differential equations is derived by adding Eqs. (30), (31) and (32a). The system is augmented by (32b). Thus,

12

$$\sum_{i=1}^{2}(-1)^{i+1}\left\{\int_{x_i}^{a_i}\left(\partial_x\overline{\mathbf{v}}^{(i)}\right)^T\mathbb{A}\partial_x\mathbf{\phi}^{(i)}dx+\int_{x_i}^{a_i}\left(\overline{\mathbf{v}}^{(i)}\right)^T\mathbb{B}_1\partial_x\mathbf{\phi}^{(i)}dx+\int_{x_i}^{a_i}\left(\partial_x\overline{\mathbf{v}}^{(i)}\right)^T\mathbb{B}_2\mathbf{\phi}^{(i)}dx+\int_{x_i}^{a_i}\left(\overline{\mathbf{v}}^{(i)}\right)^T\mathbb{C}\mathbf{\phi}^{(i)}dx\right\}$$

$$+\int_{a_1}^{a_2}\left(\partial_x\overline{\mathbf{v}}^{(3)}\right)^T\tilde{\mathbb{A}}\partial_x\mathbf{\phi}^{(3)}dx+\int_{a_1}^{a_2}\left(\overline{\mathbf{v}}^{(3)}\right)^T\tilde{\mathbb{B}}_1\partial_x\mathbf{\phi}^{(3)}dx+\int_{a_1}^{a_2}\left(\partial_x\overline{\mathbf{v}}^{(3)}\right)^T\tilde{\mathbb{B}}_2\mathbf{\phi}^{(3)}dx+\int_{a_1}^{a_2}\left(\overline{\mathbf{v}}^{(3)}\right)^T\tilde{\mathbb{C}}\mathbf{\phi}^{(3)}dx \qquad (33\text{a})$$

$$+\sum_{i=1}^{2}\left\{\left[\left(\mathbf{v}^{(3)}\right)^T\mathbb{P}-\left(\mathbf{v}^{(i)}\right)^T\mathbb{A}\right]\mathbf{\Lambda}^{(i)}\right\}_{x=a_i}=-\int_{a_1}^{a_2}\left\{\left(\partial_x\overline{\mathbf{v}}^{(3)}\right)^T\mathbb{G}_1+\left(\overline{\mathbf{v}}^{(3)}\right)^T\mathbb{G}_2\right\}dx.$$

and,

$$\left(\mathbf{\Xi}^{(i)}\right)^T\left[\mathbb{P}^T\mathbf{\phi}^{(3)}-\mathbb{A}\,\mathbf{\phi}^{(i)}-\tilde{\mathbb{F}}_i\right]_{x=a_i}=0 \quad,\text{ for }i=1,2\ . \qquad (33\text{b})$$

The system is supplemented by the following boundary conditions at the truncation boundaries $x=x_i$, for $i=1,2$,

$$\left[\mathbb{A}\,\mathbf{\phi}^{(i)}+\mathbf{k}^{(i)}\mathbb{A}\mathbf{\phi}^{(i)}\right]_{x=x_i}=0,\ i=1,2, \qquad (33\text{c})$$

where the diagonal matrix $\mathbf{k}^{(i)}=\mathrm{diag}(-1,-jk_0^{(i)},k_1^{(i)},k_2^{(i)},...,k_{N_m-1}^{(i)})$ contains the solutions of dispersion relation Eq. (23b) at $x=x_i$ for $i=1,2$ respectively. Equations (33c) are derived from the substitution of Eq. (25) in condition Eq. (16f) and their integration over local depth. Notably, the depth is assumed constant, and thus $\partial_x h=0$ at $x=x_i$, which renders $\varphi_{-1}^{(i)}(x_i)=\partial_x\varphi_{-1}^{(i)}(x_i)=0$.

The employment of auxiliary functions for the satisfaction of the continuity requirements between subregions increases the number of equations resulting in the augmented system of one-dimensional ordinary differential equations described by Eqs. (33). The imposed continuity for the velocity potential functions $\varphi^{(i)}$, $i=1,2,3$, in each subregion translates into appropriate jump conditions $\varphi_n^{(i)}-\varphi_n^{(3)}=\left[\!\left[\varphi_n^{(i)}\right]\!\right]_{a_i}\neq0$ for the

corresponding modal amplitudes at the fictitious interfaces $x=a_i$. The discontinuity condition for the modal amplitude functions is weakly by means of Lagrange multipliers.

Notably, the matrix coefficients in Eqs. (33a) are continuous functions of x involving the local expressions for the eigenbases $\mathbf{Z}$ and $\mathbf{Y}$. The latter fact is contingent to the employed depth function being sufficiently smooth (C^1).

3.4 FEM implementation

For the solution of the weak problem Eqs. (33) the classical Bubnov-Galerkin FEM approach is followed, see Zienkiewicz and Taylor, (2005). To derive the discrete form of the problem in the employed ansantz, the nodal unknowns at the rth node of the kth element contains the N_m unknown x-dependent modal amplitudes at the given subregion $i=1,2,3$, denoted $\mathbf{U}_r^{(i)}=\left(\varphi_{-1r}^{(i)},\varphi_{0r}^{(i)}...,\varphi_{N_mr}^{(i)}\right)^T$ is considered. Consequently, the restriction of the approximation of the unknowns in the kth element is written as,

$$U_k^{(i)}(x)=\sum_{r=1}^{N}L_r(x)\mathbf{U}_r^{(i)}, \qquad (34)$$

13

with N being the number of nodes within the employed element, and L_i being the Langrangian shape functions achieving $(N-1)$ degree interpolation of the nodal unknowns within the kth element. The compound vector of the kth element unknowns is written as $\mathbf{U_k}^{(i)} = \left(U_1^{(i)}, U_2^{(i)} ..., U_N^{(i)}\right)^T$ and the element restriction is rewritten as,

$$U_k^{(i)} = \mathbf{N}\mathbf{U_k}^{(i)} \ , \tag{35}$$

by means of the array $\mathbf{N}$,

$$\mathbf{N}_{(N_m+2)\times N(N_m+2)} = \left[\begin{array}{ccccc} L_1\mathbf{I}_{N_m+2} & | & L_2\mathbf{I}_{N_m+2} & | & .... & | & L_{N-1}\mathbf{I}_{N_m+2} & | & L_N\mathbf{I}_{N_m+2} \end{array} \right].$$

Substituting Eq. (35) in Eq. (33) and letting weight functions to coincide with Lagrangian shape functions, i.e. $\mathbf{v}^{(i)}$, $\mathbf{\Xi}^{(i)} \equiv \mathbf{N}$, $i = 1,2,3$, the following expressions for the element matrices and forcing vector in their corresponding discretised subregions are produced,

$$\mathbb{K}_e^{(i)} = \int_e (\partial_x\mathbf{N})^T \mathbb{A}(\partial_x\mathbf{N}) \ dx + \int_e \mathbf{N}^T\mathbb{B}_1(\partial_x\mathbf{N}) \ dx \ + \int_e (\partial_x\mathbf{N})^T \mathbb{B}_2\mathbf{N} \ dx + \int_e \mathbf{N}^T\mathbb{C}\mathbf{N} \ dx \tag{36a}$$

$$\mathbb{K}_e^{(3)} = \int_e (\partial_x\mathbf{N})^T \tilde{\mathbb{A}}(\partial_x\mathbf{N}) \ dx + \int_e \mathbf{N}^T\tilde{\mathbb{B}}_1(\partial_x\mathbf{N}) \ dx \ + \int_e (\partial_x\mathbf{N})^T \tilde{\mathbb{B}}_2\mathbf{N} \ dx + \int_e \mathbf{N}^T\tilde{\mathbb{C}}\mathbf{N} \ dx \tag{36b}$$

$$\mathbb{F} = -\int_e \left\{(\partial_x\mathbf{N})^T \mathbb{G}_1 + \mathbf{N}^T\mathbb{G}_2\right\}dx \tag{36c}$$

At the interfacial nodes, located at $x = a_i$, the discrete multipliers are contained in the vector as $\mathbf{\Lambda}^{(i)} = \left(\lambda_1^{(i)}, \lambda_2^{(i)} ..., \lambda_{N_m+2}^{(i)}\right)^T, i = 1,2$. Next, we distinguish between the *dofs* in each of the sub-regions as $\mathbf{U}^{(i)}$, $i = 1,2,3$, contained in the vector of global unknowns $\mathbf{u} = \left[\mathbf{U}^{(1)} \quad \mathbf{U}^{(3)} \quad \mathbf{U}^{(2)}\right]^T$, while the additional *dofs* associated with discrete Lagrange multipliers are contained in vector $\mathbf{\lambda} = \left[\mathbf{\Lambda}^{(1)} \quad \mathbf{\Lambda}^{(2)}\right]^T$. The employment of Lagrange multipliers increases the total $(N_m+2)\times N$ system unknowns by $2\times(N_m+2)$.

After assembly, by means of the element matrices in Eqs. (36), the system corresponding to Eqs. (32), (33) take the form of a discrete saddle point problem with respect to $\mathbf{u}$ and $\mathbf{\lambda}$ (*see* Benzi et al., 2005),

$$\mathbf{Au} + \mathbf{B}^T\mathbf{\lambda} = \mathbf{F} \quad \text{and} \quad \mathbf{Bu} = \mathbf{g} \ . \tag{37}$$

The above system of discrete algebraic equations assumes the following form,

$$\left[\begin{array}{ccc|c} \mathbb{K}^{(1)} & & & \\ & \mathbb{K}^{(3)} & & \mathbf{B}^T \\ & & \mathbb{K}^{(2)} & \\ \hline - & - & - & | & - \\ & \mathbf{B} & & 0 \end{array}\right] \left[\begin{array}{c} \mathbf{U}^{(1)} \\ \mathbf{U}^{(3)} \\ \mathbf{U}^{(2)} \\ \hline \mathbf{\lambda} \end{array}\right] = \left[\begin{array}{c} \mathbf{F} \\ \hline \mathbf{g} \end{array}\right]$$

Matrix $\mathbf{A}$ is symmetric, as a consequence of the employed Bubnov-Galerkin approach, while the system retains its symmetry due to the geometric conformity of the interfaces. The solution of the above system recovers the unknown complex amplitude functions $\varphi_n^{(i)}(x)$ in each subregion and the wave fields are eventually calculated by means of Eqs. (26) and (30), with the imposed continuity conditions being satisfied weakly by means of the employed Lagrange multiplier formulation.

14

A system of the form Eq. (37) needs to be solved for each radiation-type problem. It is important to note however that the matrix coefficients introduced in Eqs. (33), which are parametrically defined along x, can be calculated once in advance for a given bathymetric profile and spatial. Moreover, matrices, $\mathbf{A}$, $\mathbf{B}$ of Eq. (37) can also be calculated once for a given spatial mesh and FEM approximation. This attribute of the method significantly reduces the number of operations. On the other hand, the forcing vector $\mathbf{F} = \begin{bmatrix} 0 & \mathbb{F} & 0 \end{bmatrix}^T$ and constraints vector $\mathbf{g} = \begin{bmatrix} \tilde{\mathbb{F}}_1 & \tilde{\mathbb{F}}_2 \end{bmatrix}^T$ contain the upper surface Neumann data $V(x)$ on the plate–covered region and need to be constructed for each sub-problem. It is noted that the FEM implementation allows for the construction of a p-adaptive scheme that would increase the polynomial degree for sub-problems corresponding to highly oscillatory structural modes. However the latter would require the reconstruction of matrices $\mathbf{A}$, $\mathbf{B}$ between p-refinements.

4 Solution for the hydroelastic response and the total wavefield

In the previous section, the weak formulation and FEM approximation of each radiation-type problem is presented. The solution of system (35), produces the modal amplitude functions $\boldsymbol{\varphi}^{(i)} = \left\{ \varphi_n^{(i)}(x), \, n = -1,0,1,2,..... \right\}$ for the diffraction and the ℓth radiation wavefield, excited by the corresponding 'dry' mode of the free plate. By iteration, N_f radiation problems corresponding to N_f flexural modes need to be solved. Notably, the numerical computations for the decoupled problems can be carried out in parallel.

Subsequently, as described in Section 2, in order to obtain the total wavefield solution and the deflection of the floating plate, the unknown complex amplitudes c_ℓ, involved in the radiation wavefield and structural deflection expansions, need to be calculated. This is achieved through the satisfaction of the pressure equilibrium condition on $\Gamma_f^{(3)}$, Eqs. (13). A Galerkin scheme is proposed for the treatment of pressure equilibrium Eqs. (13), involving the dynamic response of thin or thick plate structures described by Eqs. (14) and (15) respectively.

4.1 Kirchhoff-Love plate

On $\Gamma_f^{(3)}$, it holds

$$\partial_{xx}\left[D(x)\partial_{xx}w \right] + \left(\rho_w g - \omega^2 \rho_e \tau(x) \right)w = i\omega\rho_w \left(\varphi_R + \varphi_D \right)\big|_{z=0} , \tag{38}$$

and the corresponding eigenvalue problem for the free plate ends reads,

$$\partial_{xx}\left[D(x)\partial_{xx}w \right] - \omega_\ell^2 \rho_e \tau(x) w_\ell = 0 , \tag{39}$$

where ω_l^2 and w_l are the eigenvalues and eigenmodes of the structrure. Substituting Eq. (39) in Eq. (38) and considering Eqs.(13) and (14), the dynamic condition results in

$$\sum_\ell^{N_f} c_\ell \left[\left\{ \rho_e \tau(x)\left(\omega_\ell^2 - \omega^2 \right) + \rho g \right\} w_\ell - i\omega\rho\,\varphi_\ell\big|_{z=0} \right] = i\omega\rho\varphi_D\big|_{z=0} . \tag{40}$$

By means of the eigenbasis, $\left\{ w_\ell(x), \, l = 1,2,... \right\}$, calculated by FEM, the decoupling of Eq. (38) is achieved resulting in the following $N_f \times N_f$ system with the unknown amplitudes contained in the vector $\mathbf{C}_\ell$,

15

$$\left(\mathbf{A}^{\mathrm{K}}\,\mathbf{diag}\left(\omega_{\ell}^{2}-\omega^{2}\right)+\mathbf{B}^{\mathrm{K}}\right)\mathbf{C}_{\ell}=\mathbf{F}^{\mathrm{K}} \tag{41}$$

while the matrix coefficients are given by,

$$\mathbf{A}_{m\ell}^{\mathrm{K}}=\int_{a_{1}}^{a_{2}}\rho_{e}\tau(x)w_{m}w_{\ell}\ dx,\ \mathbf{B}_{m\ell}^{\mathrm{K}}=\rho_{w}g\int_{a_{1}}^{a_{2}}w_{m}w_{\ell}\ dx-i\omega\rho_{w}\int_{a_{1}}^{a_{2}}w_{m}\left.\varphi_{\ell}\right|_{z=0}\ dx,\ \mathbf{F}_{m}^{\mathrm{K}}=i\omega\rho\int_{a_{1}}^{a_{2}}w_{m}\left.\varphi_{D}\right|_{z=0}\ dx.$$

The solution of system (41) will retrieve c_{ℓ}, employed for the calculation of $w(x)$ and $\varphi_{R}(x,z)$ and finally total wavefield solution $\varphi(x,z)$, through Eqs. (1), (2) and (3). Consequently, the bending moment and shear force distributions along the structure can be subsequently calculated respectively as,

$$M(x)=-D(x)\partial_{xx}w(x)\ ,\ \ S(x)=-\partial_{x}\left(D(x)\partial_{xx}w(x)\right)\ . \tag{42}$$

4.2 Mindlin plate

For the case of an inhomogeneous Mindlin plate under cylindrical bending the vertical plate motion is governed by a coupled system of equations in terms of the unknown the plate deflection and rotation. Ti treat the above complexity a field elimination by means of the numerically computed eigenbases, $\{w_{\ell}(x),\ \ell=1,2,...,N_{f}\}$ and $\{\theta_{\ell}(x),\ \ell=1,2,...,N_{f}\}$ is performed.

Notably, the unknown fields in Eqs. (13) and (15) expressing motion equilibrium, are represented as already mentioned by means of Eq. (1) and (2) $w(x)=\sum_{\ell}^{N_{f}}c_{\ell}w_{\ell}(x)\ ,\ \ \varphi_{R}(x)=\sum_{\ell}^{N_{f}}c_{\ell}\varphi_{\ell}(x)$, while rotation is written as $\theta(x)=\sum_{\ell}^{N_{f}}d_{\ell}\theta_{\ell}(x)$.

To derive the coupling between complex amplitudes c_{ℓ} and d_{ℓ}, Eqs (13b,15b) is rewritten upon substitutions as,

$$\sum_{\ell}^{N_{f}}c_{\ell}\left[-\omega^{2}I_{\rho}d_{\ell}\theta_{\ell}-\kappa G\tau\left(c_{\ell}\partial_{x}w_{\ell}-d_{\ell}\theta_{\ell}\right)-\partial_{x}\left[Dd_{\ell}\partial_{x}\theta_{\ell}\right]\right]=0 \tag{43}$$

Next, Galerkin's method employing $\theta_{\ell}(x)$ as test functions, performing integration by parts and finally resorting to matrix notation yields the following expression,

$$\mathbf{d}_{\ell}=\mathbf{C}_{m\ell}^{M}\mathbf{c}_{\ell}\,, \tag{44}$$

with ,

$$\mathbf{C}_{m\ell}^{M}=\left(-\omega^{2}\int_{a_{1}}^{a_{2}}\theta_{m}I_{\rho}(x)\theta_{\ell}\ dx+\int_{a_{1}}^{a_{2}}\theta_{m}\kappa G\tau(x)\theta_{\ell}\ dx+\int_{a_{1}}^{a_{2}}\partial_{x}\theta_{m}D(x)\partial_{x}\theta_{\ell}\ dx\right)^{-1}\left(\int_{a_{1}}^{a_{2}}\theta_{m}\kappa G\tau(x)\partial_{x}w_{\ell}dx\right)$$

Equation (13a), upon substitution of Eq. (15b) is similarly rewritten as,

$$\sum_{\ell=1}^{N_{f}}\left[\left(\rho g-\omega^{2}\rho_{e}\tau\right)c_{\ell}w_{\ell}-\partial_{x}\left[\kappa G\tau\left(c_{\ell}\partial_{x}w_{\ell}-\theta\right)\right]\right]=i\omega\rho\left.\Phi_{D}\right|_{z=0}+\sum_{\ell=1}^{N_{f}}i\omega\rho\left.c_{\ell}\varphi_{\ell}\right|_{z=0} \tag{45}$$

Next, Eq. (45) is tested with $w_\ell(x)$ and after integration by parts and substituting Eq. (44) the following system is obtained,

$$\mathbf{A}_{m\ell}^M \, \mathbf{c}_\ell = \mathbf{F}_\ell \,, \tag{46}$$

with matrix $\mathbf{A}_{m\ell}^M = \mathbf{a}_{m\ell}^M - \mathbf{b}_{m\ell}^M \mathbf{C}_{m\ell}^M - \mathbf{d}_{m\ell}^M$ and $\mathbf{F}_\ell = \int_{a_1}^{a_2} i\omega\rho\, w_m \Phi_D\big|_{z=0} \, dx$,

while, $\mathbf{a}_{m\ell}^M = \left(-\omega^2 \int_{a_1}^{a_2} w_m \rho_e \tau(x) w_\ell \, dx + \int_{a_1}^{a_2} w_m \rho_w g(x) w_\ell \, dx + \int_{a_1}^{a_2} \partial_x w_m \kappa G\tau(x) \partial_x w_m \, dx \right)$ and

$$\mathbf{b}_{m\ell}^M = \int_{a_1}^{a_2} \partial_x w_m \kappa G\tau(x)\theta_\ell \, dx, \; \mathbf{d}_{m\ell}^M = \int_{a_1}^{a_2} i\omega\rho\, w_m \varphi_\ell\big|_{z=0} \, dx \,.$$

The solution of system Eq. (46) will retrieve c_ℓ, employed for the calculation of $w(x)$, $\varphi_R(x,z)$ and the composition of the total wave-field solution $\varphi(x,z)$. The bending moment and shear force distributions can be subsequently calculated by means Eq. of respectively as,

$$M(x) = -D(x)\partial_x \theta(x) \,, \qquad S(x) = \kappa G\tau\left(\partial_x w(x) - \theta(x)\right). \tag{47}$$

The reflection and transmission coefficients (A_R, A_T) in terms of the total wave-field are calculated by means of the upper surface solution at domain edges $x = x_i$, $i = 1, 2$, as,

$$|A_R| = \left[\varphi(x_1, 0) - \exp(jk_0^{(1)}x_1)\right]\exp(jk_0^{(1)}x_1) \,, \tag{48a}$$

$$|A_T| = \varphi(x_2, 0)\exp(jk_0^{(2)}x_2) \,. \tag{48b}$$

4.3 Structural Eigenvalue problems

The proposed methodology implements a 'dry' mode expansion for the vertical deflection of the elastic body. The calculation of the *in vacuo* plate modes and natural frequencies requires the solution of a structural eigenvalue problem formulated for the Classical Thin plate theory (Kirchhoff-Love) or the 1st order shear deformation theory of Mindlin plates under cylindrical bending. The solution to the structural eigenvalue is treated separately from the hydrodynamics, as already discussed in a previous section. In the present work, the finite element method was employed in order to implement inhomogeneity effects in a straightforward manner. For the Kirchhoff plate, the conventional variational formulation and C^1 elements featuring Hermite interpolation are employed (see Papathanasiou et al., 2015). For the approximation of the inhomogeneous Mindlin plate eigenvalue problem, a C^0 variational approach is adopted, featuring Lagrange shape functions, in order to avoid the use of non-conforming elements. The aforementioned approach is prone to locking effects, unless a high interpolation order is attained (Hughes, 2000). Notably, despite the fact that *p*-refinement significantly increases the employed degrees of freedom, the 1-D eigenvalue problem remains computationally inexpensive and thus the employed brute force approach is justified. Moreover, the eigenvalue problem needs only to be solved once for each structural configuration. For the sake of completeness, details of the FEM implementation for the solution of the inhomogeneous structural eigenvalue problems are provided in Appendices A and B.

5   Numerical results and discussion

In the present section, the performance and accuracy of the present method is examined in a series of 2D cases. First, the hydroelastic response of a thin, homogeneous plate and the corresponding wavefield transformations in an example configuration featuring an abruptly varying seabed, are considered in order to illustrate the key features of the method in isolation of other inhomogeneities, i.e. variable thickness.

Next, comparisons with published results for a range of parameters are carried out. Considered cases involve both Kirchhoff and Mindlin plate models over constant (deep, intermediate and shallow water cases) and variable seabed, as well as thickness variability. Throughout this section and for all presented examples, the water density is s, $\rho_w = 1025 \text{ kg} \cdot m^{-3}$, unless stated otherwise, and the acceleration of gravity as $g = 9.81 \, m \cdot s^{-2}$.

5.1   The case of a uniform, thin plate over arbitrarily varying seabed

The case of a shoaling bathymetric profile is initially considered in order to illustrate the full features of the proposed method. In the following example, the fluid region is defined as $\Omega : (x,z) \in (-230\text{m}, 230\text{m}) \times (-h(x), 0)$ with the bathymetric profile given as the superposition $h(x) = g_1(x) + g_2(x)$, with

$$g_1(x) = (h^- + h^+)/2 - (h^- - h^+)/2 \tanh\left(2\pi(x/205 + 0.0014) - 0.5\right), \tag{49}$$

$$g_2(x) = 0.7\sin(k_b x)\exp\left(-10^{-4} x^2\right), \quad \text{while} \quad k_b = 2\pi/\lambda_b \text{ and } \lambda_b = 25.625 \text{ m} \tag{50}$$

The profile $h(x)$ corresponds to a corrugated, shoaling region; see Fig.2. In the above equations, $h^- = 13\,m$ and $h^+ = 7\,m$ correspond to the constant depth levels at the farfield. The homogeneous floating structure is extending in $-L/2 < x < L/2$ with $L = 120\,m$ being the length of the plate. An incident wavefield propagating towards the positive x axis with frequency $\omega = 1.4\,rad/s$ is considered to excite the floating structure. Since, $k^- h^- = 2.6248$ and $k^+ h^+ = 1.5348$, the set example falls outside the limits of either deep or shallow water wave theory. The thickness of the employed structure is assumed constant $\tau = 1\,m$, suggesting a thickness-to-length ratio $\tau/L = 0.0083$ well within the range of application of the Classical Thin Plate theory, allowing the plate to be modelled under the Kirchhoff-Love assumptions. The material properties of the structure are taken as $E = 5$ GPa, $\nu = 0.3$ and density $\rho_e = 922.5 \text{ kg/m}^3$, corresponding to sea ice (see for example Bennetts et al. (2007); Porter and Porter, (2000); Smith and Meylan (2011) and others). The presented method, keeping $N_m = N_f = 15$ number of terms in the series expansions Eqs. (1) and (2) to ensure convergence, is employed for the calculation of the hydrodynamic characteristics of the wave-field and the response of the structure. The latter suggests the employment of 13 evanescent modes in the vertical hydrodynamic expansion, in addition to the propagating and sloping bottom modes and 13 flexural modes in the elastic expansion, in addition to rigid body modes. Linear Lagrange elements are used for the representation of the discrete system Eq. (37), while a total of 44 elements per mean incident wavelength are employed. Results convergence was assessed in the sense that consecutive mesh refinements rendered negligible residuals.

In Fig. 2 the equipotential lines, corresponding to the real part of the computed solutions of the component hydrodynamic problems are shown, while in Fig.3, the corresponding plot for the composed total velocity potential is drawn. At the bottom of Fig. 3, close-ups of the wave-field solution at the edges of the plate are given. Equipotential lines in the above figures are seen to intersect the bottom normally, satisfying the Neumann condition on the seabed (Eq. 10).
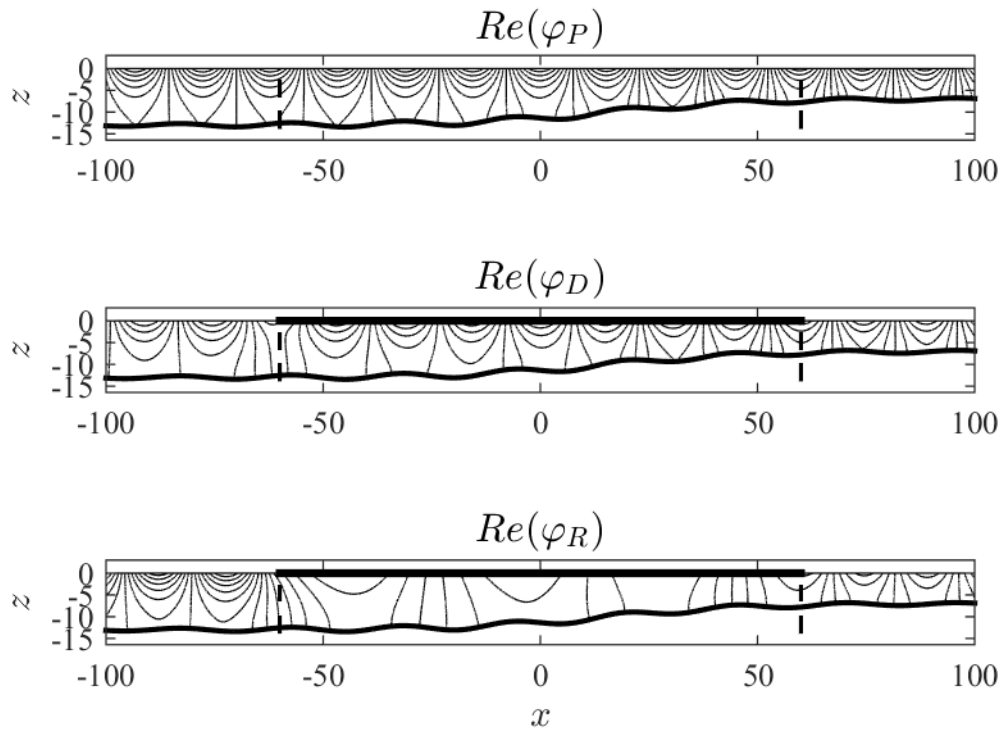
Fig. 2. Real part of the solutions to the component propagation (top), diffraction (middle) and radiation problems (bottom)
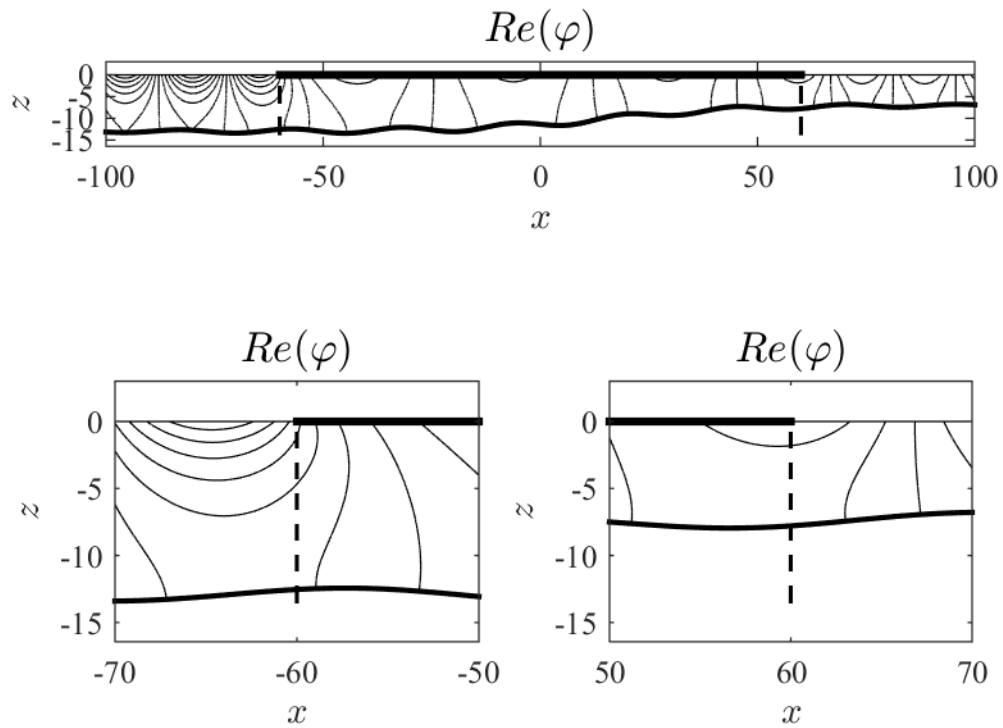
Fig. 3. Real part of the total solution (top), fictitious interfaces between subregions (bottom)
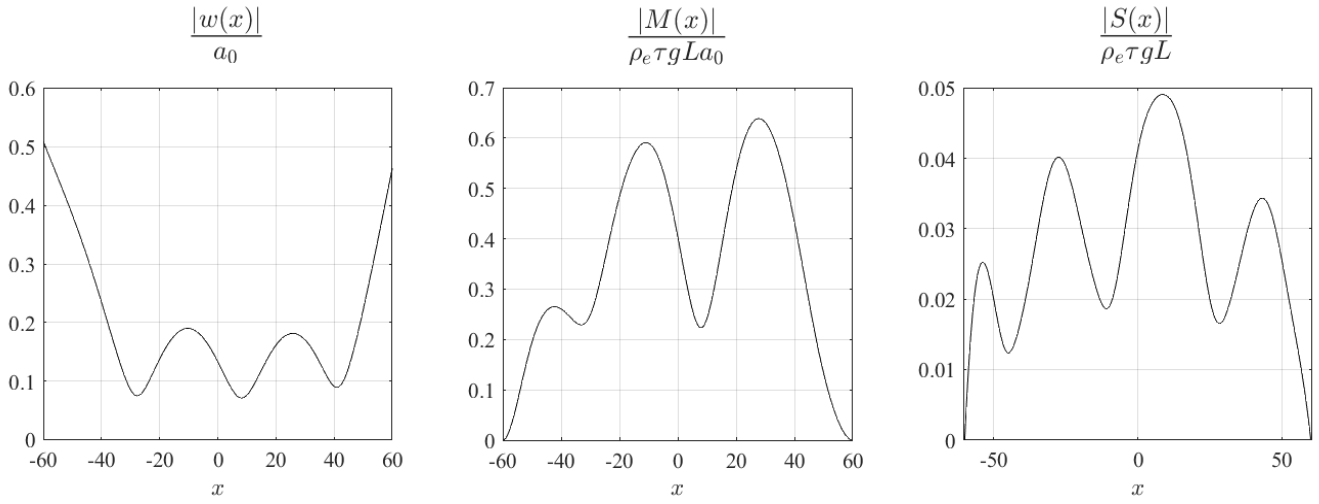
Fig. 4. Non-dimensionalised moduli of plate deflection (left), bending moment (middle), shear force (right)
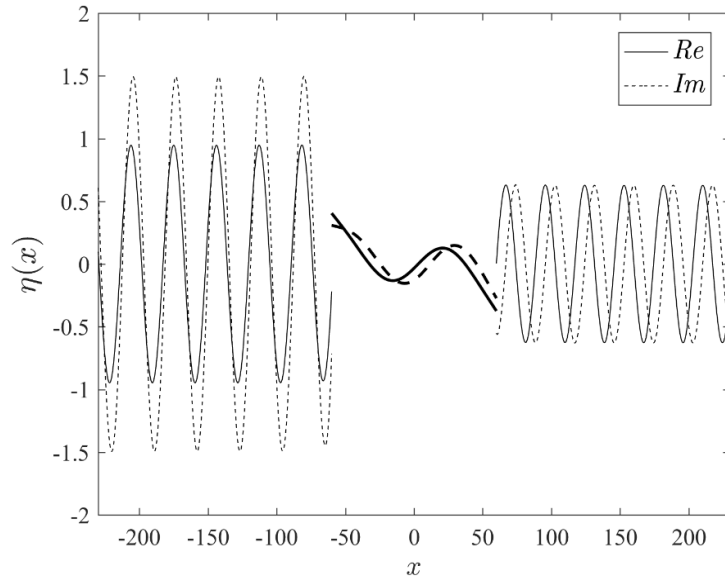
Fig. 5. Real and imaginary parts of free surface elevation $\eta(x)$ and plate deflection $w(x)$, denoted by a thicker line.

Moreover, the matching of the velocity potential and flux on the fictitious interfaces between subregions, depicted by dashed lines, is excellent for radiation-type and total wave-field solutions, as illustrated in Fig. 3, suggesting that the weak satisfaction of transmission conditions adequately captures local scattering phenomena at the plate edges and the employed vertical expansion satisfies energy flux conservation across interfaces. Next, the normalized to the wave amplitude modulus of the plate deflection, and the normalized absolute moment and shear force for the given example are plotted in Fig. 4. Notably, the satisfaction of the zero moment and zero shear conditions at the free edges of the plate, observed at Fig. 4, is *a priori* guaranteed by the employment of the *in vacuo* modes, which is an advantage of the approach. The latter becomes more apparent in the 3 D extension of the proposed method, where the satisfaction of plate edge conditions is computationally intensive and not trivial in general geometries. Finally, in Fig. 5 the real and imaginary parts of the solution for the normalized with respect to incident amplitude free surface elevation $\eta(x) = i\omega g^{-1}\varphi(x,0)$, $x \in (x_1, a_1) \cup (a_2, x_2)$ and plate deflection $w(x)$, $x \in (a_1, a_2)$ are plotted.

20

Next, in order to explore the effects of modal truncation in the expansion Eq. (1), the computed amplitudes c_ℓ are considered for the above example. In Table 1, the first 11 moduli of the computed mode amplitudes c_ℓ are presented. For the computations, $N_m = 15$ vertical modes are employed for the hydrodynamic series expansion while a varying number of flexural modes , $N_f = 15, 20, 30$ in the modal expansion is considered. It is evident, that in the present case, fourth mode (2nd flexural mode) is dominant while after the 8th mode the corresponding amplitudes are less than 1% of the maximum mode amplitude $|c_4|$, which is indicative of the rapid convergence of the modal expansion.

Table 1 Non-dimensional complex amplitudes c_ℓ

					$\|c_\ell\|$						
ℓ :	1	2	3	4	5	6	7	8	9	10	11
$N_f = 15$	13.7960	41.3947	20.6474	51.7936	23.5340	5.9249	0.4174	0.6211	0.0593	0.1287	0.0165
$N_f = 20$	13.7961	41.3947	20.6474	51.7931	23.5341	5.9247	0.4174	0.6211	0.0593	0.1286	0.0165
$N_f = 30$	13.7961	41.395	20.6475	51.7927	23.5339	5.9245	0.4174	0.621	0.0593	0.1286	0.0165

In Fig. 6, the integrated over the spatial domain moduli of the complex amplitude functions $\|\varphi_n\|_{1,(x_1,x_2)} = \int_{x_1}^{x_2} |\varphi_n(x)| dx$, calculated for the component hydrodynamic problems (incident φ_P, diffraction φ_D and ℓ^{th} radiation problem) as well as the total solution amplitudes, calculated as $\varphi = \varphi_P + \varphi_D + \sum_{\ell=1}^{N_f} c_\ell \varphi_R$ are comparatively plotted. A total of $N_f = 15$ bending modes were employed in the modal expansion of the plate. The y-axis is in logarithmic scale while the x-axis shows the increasing number of vertical modes, n. Notably, the modal amplitude decay rate for the propagating wavefield φ_P is $O(n^{-4})$, while the corresponding rates of decay concerning the diffraction solution and the ℓth radiation potential solution φ_ℓ appear to be smaller $O(n^{-3+\varepsilon})$, $\varepsilon < 1$. In the case of the incident wavefield φ_P over an abruptly sloping seabed, the above is in agreement with the findings in Athanassoulis and Belibassakis (1999).

In the aforementioned work, it was shown that the enhanced representation for the wave potential, including the additional sloping bottom mode Z_{-1} features an accelerated rate of convergence $O(n^{-4})$, compared to the standard representation $O(n^{-2})$ that fails to accurately account for bottom slope effects.
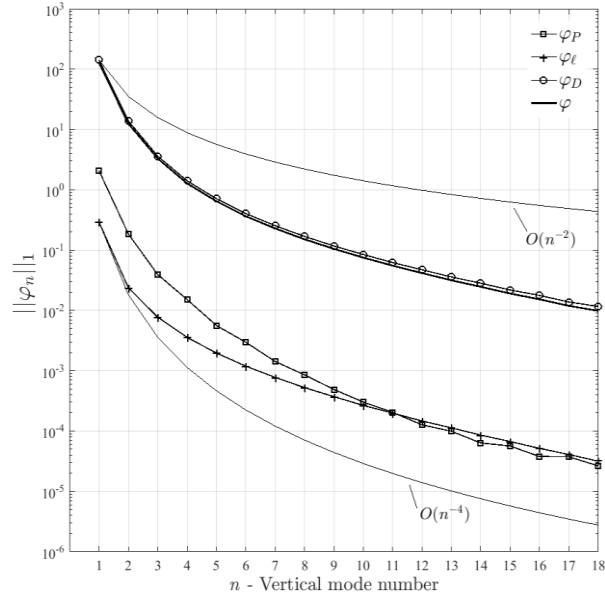
Fig. 6. Integrated moduli $\|\varphi_n\|_1 = \int_{x_1}^{x_2} |\varphi_n(x)| dx$ of the modal amplitude functions for component hydrodynamic

solutions *vs* mode number n

The inclusion of the additional mode allows for the consistent satisfaction of the bottom boundary condition, ensuring the absolute and uniform convergence up to the boundaries. The reduced order of decay of the modal amplitudes for the radiation-type wavefields and in extend for the total solution is attributed to the weak satisfaction of the interface conditions.

5.2 Validation of methodology

For the validation of the proposed methodology, a series of comparisons with results presented in the literature are performed. For the numerical approximations presented in this section by means of the proposed methodology, $N_m = 15$ modes are kept in the vertical expansion, including the additional sloping bottom mode, while $N_f = 15$ bending modes are kept in the deflection representation

5.2.1 Constant depth

(a) Homogenous thin plate case

The hydroelastic response of a homogeneous thin plate over variable bathymetry is initially compared against the results documented in Belibassakis and Athanassoulis (2005). In the former work, the consistent coupled mode system, proposed by the authors in an earlier contribution, is extended to account for the hydroelastic problem. The analysis is restricted to homogeneous, thin plates and bathymetric variations that are restricted to the plate-covered region. In the following examples, the plate is assumed to extend infinitely in the y-direction, undergoing cylindrical bending under harmonic wave action and the length of the plate is $L = 500m$. In the paper, the plate mass effect is considered negligible and ignored, thus the available data for their analysis are limited to the flexural rigidity of the floating body, $D/\rho_w g = 10^5 m^4$.
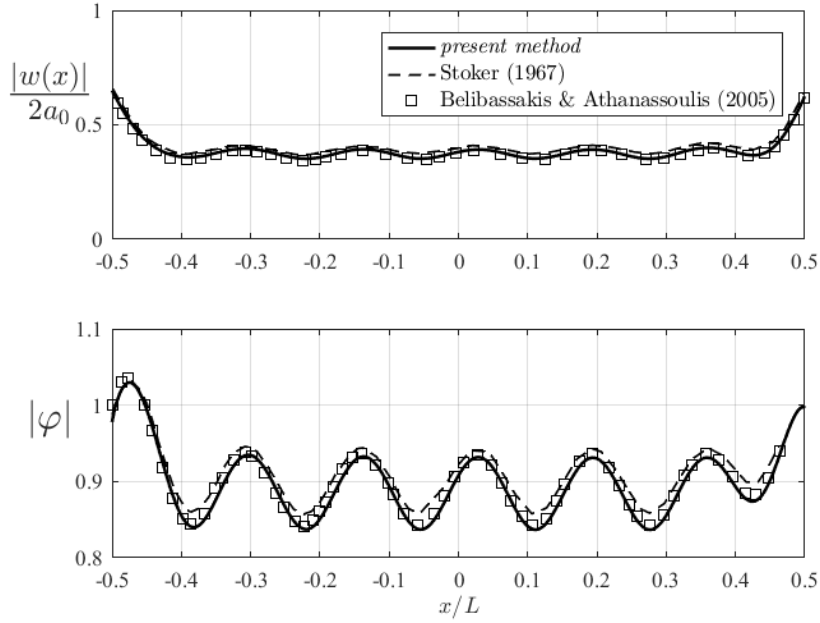
Fig. 7 Hydroelastic solution in constant depth and almost shallow water conditions. (a) Normalised deflection to the waveheight (top). (b) Modulus of the velocity potential on the plate. Solid line denotes the present mehtod, dashed line the solution of Stoker's shallow raft model and squared the solution by Belibassakis and Athanassoulis (2005)

The above premise in unphysical is our case and thus, the set flexural rigidity $D/\rho_w g = 10^5 m^4$ is assumed to correspond to a body with constant thickness $\tau = 1.3$ m and material characteristics $E = 5$ GPa, $v = 0.3$ and density $\rho_e = 922.5$ kg/m^3, following Bennetts et al. (2007). The slenderness of the structure falls well within the limits of the classical plate theory while the material characteristics model sea ice. In the examined scenario, the incoming wave frequency is $\omega = 0.4$ rad/s and the constant depth is $h = 10$ m, which reduces the depth-to-incident wavelength ratio to $h/\lambda = 0.066$, approximating shallow wave conditions. Comparisons in terms of the normalized plate deflection to the wave height $|w(x)|/2a_0$ and the modulus of the potential on the plate $|\varphi(x,z=0)|$ are shown in Fig. 7. For the discretization of the hydroelastic region, 250 linear Lagrange elements were employed. The above figure illustrates the results of the present method, shown by a solid line, against the hydroelastic CMS solution by Belibassakis and Athanassoulis (2005) and shallow–water thin raft model by Stoker (1967) denoted by a dashed line. The results are found in excellent agreement, verifying the behavior of the proposed method in shallow water conditions.

Next, a second case, corresponding to deep water conditions, originally presented in Tagaki et al. (2000) is examined. The case explored in was validated against the eigenfunction matching technique by Yoshimoto (1997) and later found in good agreement with the results in Hermans (2003). The examined plate has length $L = 1.4$ m and flexural rigidity $D/\rho_w g = 1.74 \cdot 10^{-3} L^4$ m^4, while it floats over constant depth $h = 0.5$ m.
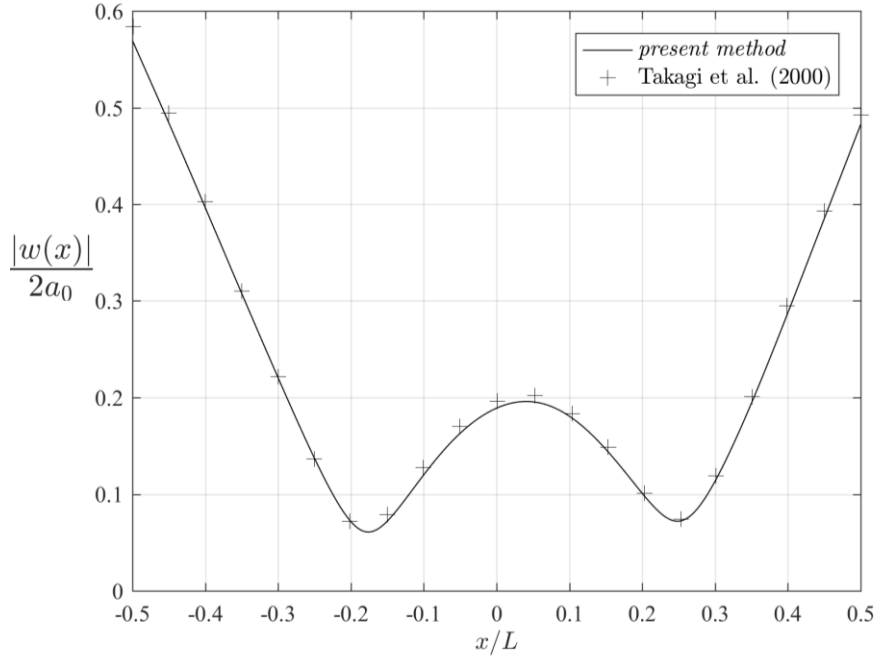
Fig. 8. Normalised deflection of floating elastic plate in deep water. Solid line denotes the solution obtained by means of the present method, while crosses denote the solution in Takagi et al. (2000).

The normal incident wave-field has angular frequency $\omega = 4\pi$ rad s^{-1}. The plate parameters are chosen as $\tau = 5.2 \cdot 10^{-3}$ m, with $E = 5$ GPa, $v = 0.3$ and density $\rho_e = 922.5$ kg/m^3 to comply with case configuration as discussed in the previous example. In Fig.8, the modulus of the plate deflection normalized with respect to the incident wave height $(2a_0)$ is compared against the results presented in Takagi et al. (2000) denoted with crosses, and once again the results are in very good agreement, indicating that the present method is appropriate for all water-depth conditions.

Next, in Fig. 9 the proposed method is compared against the experimental results published in Wu et al. (1995), and originally presented in Utsunomiya et al. (1995). The examined homogeneous, thin plate features length $L = 10$ m, width $W = 0.5$ m, thickness $\tau = 0.038 m$ and draft $d = 8.36 \cdot 10^{-3}$ m. The Young's modulus $E = 103$ MPa and the density of the elastic material is $\rho_e = 220$ kg/m^3. The constant depth is set to $h = 1.1$ m. In the figure, the normalized plate displacement under three different incident wave periods is illustrated. For $T = 1.429$ s and $T = 0.7$ s the present method, denoted by a continuous line is compared against the converged results obtained by means of the vertical multi-modal approximation, accounting for variable draft, in Bennetts et al. (2007), denoted by a dashed line. Experimental results referenced in Wu et al. (1995) are noted by squares, triangles and circles for periods $T = 2.875$ s, 1.429 s and $T = 0.7$ s respectively. Notably, the geometric characteristics of the given structure suggest that its dynamic response is indeed accurately described by means of tclassical thin plate theory, since $\tau/L = 0.0038$. Furthermore even in the higher frequency case, the incident wavelength is considerably larger than the plate thickness ($\tau/\lambda \approx 0.05$) and thus shear deformation effects are rendered negligible. For $T = 1.429$ s, the obtained solutions are almost identical while minor deviations of a quantitative nature are observed for the high frequency case. This could be attributed to the fact that the present work does not account for the constant draft. Results are generally found in very good agreement with the results by Bennetts et al. (2007), illustrating the beneficial effects of evanescent mode employment in capturing scattering effects due to the edges of the plate.

24
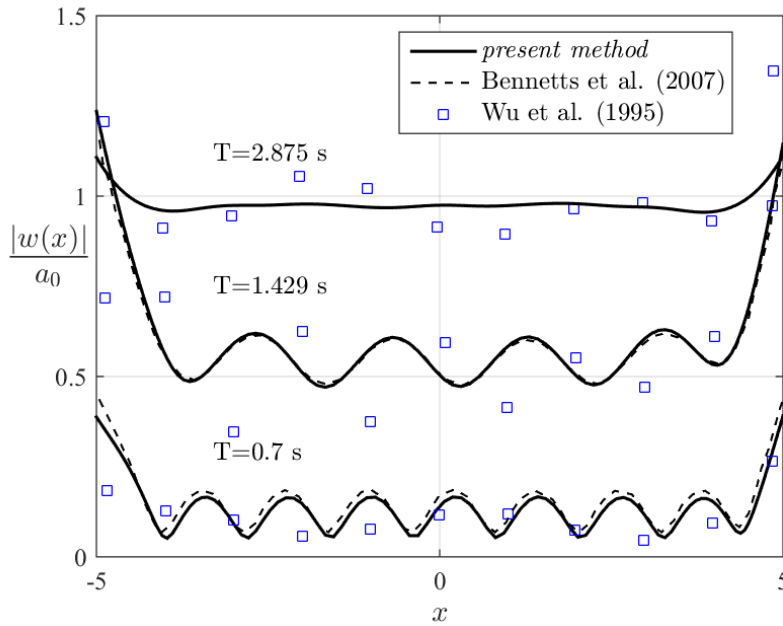
Fig. 9. Non-dimensional displacement amplitude for (a) T=2.875 s, (b) T=1.429 s and (c) T=0.7 s. Solid line denotes the solution of the present method while the dashed line indictes the results in Bennetts et al. (2007). Experimental data are denoted by squares.

(b) Homogenous thick plate case

In all cases cosnidered to this point, the Classical thin plate theory is employed and shear and rotary inerta effects are neglected. Recently, several autthors studied the diffraction of surface waves by the presence of floating this elastic plates, e.g., Zhao et al (2008). In the afforementioned paper, comparisons against the small scale test documented above (Wu et al., 1995) were performed for increasing thickness values, $\tau = 0.038$ m, 0.075 m and 0.1 m . In Fig. 10, the present method employing the Mindlin plate model compared favorably against the results in (Zhao et al., 2008) , depicted with thinner lines for each thickness values and period $T = 1.429$ s .

Notably, the dynamic response of the Kirchhoff and Mindlin plate models were almost identical even in the thicker case $\tau = 0.1$ m, where thickness-to-incident wavelength ratio is an order of magnitude smaller than thickness $(\tau/\lambda \approx 0.032)$. To illustrate the differences between the two plate models a higher frequency case, for $T = 0.5$ s is considered in Fig. 11. Again, three thickness cases thickness values, $\tau = 0.038$ m, 0.075 m and 0.1 m were considered for the same plate configuration. In the figure, the non-dimensional deflection and bending moment are calculated for both plate models, resulting to three pairs of curves corresponding to the three thickness values. The pairs are given an increasing number that match increasing thickness values. Solid lines denote the solutions obtained by the thin plate assumption, while the dashed lines indicate Mindlin plate solutions. The thickness-to-incident wavelength ratios, ranging in magnitudes $\tau/\lambda \approx 0.01 \sim 0.25$ are comparable to thickness in the examined cases, which justifies thick plate assumptions while the structure remains slender. The plate deflection and bending moment distributions shown in Fig. 11, indeed deviate due to the effects of rotary inertia and shear deformation under high frequency excitation.
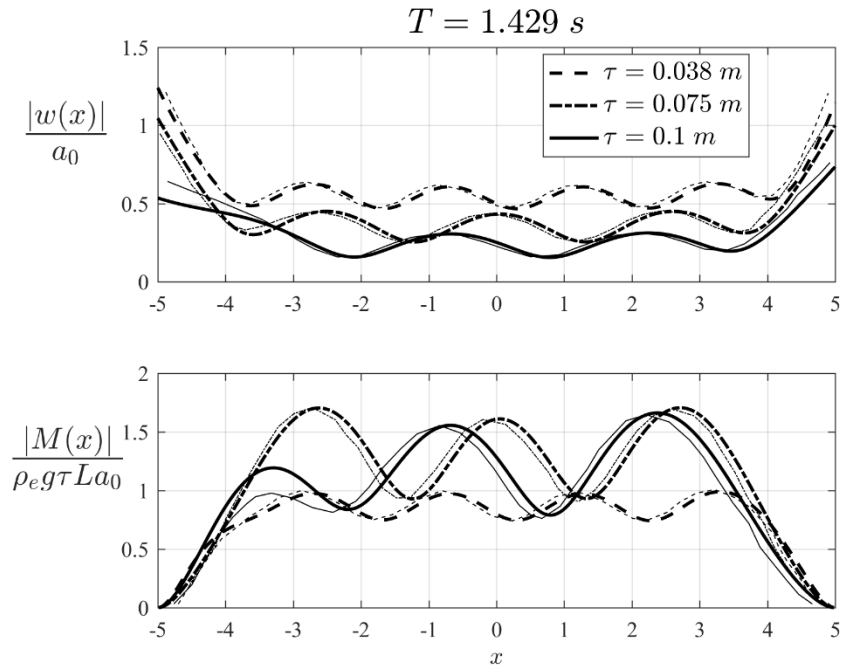
Fig. 10. Modulus of the non-dimensionalised deflection and moment for $T = 1.429\,s$ and different thickness values. Thick lines correspond to results obtained by the present method while thinner lines indicate the results in Zhao et al. (2008).
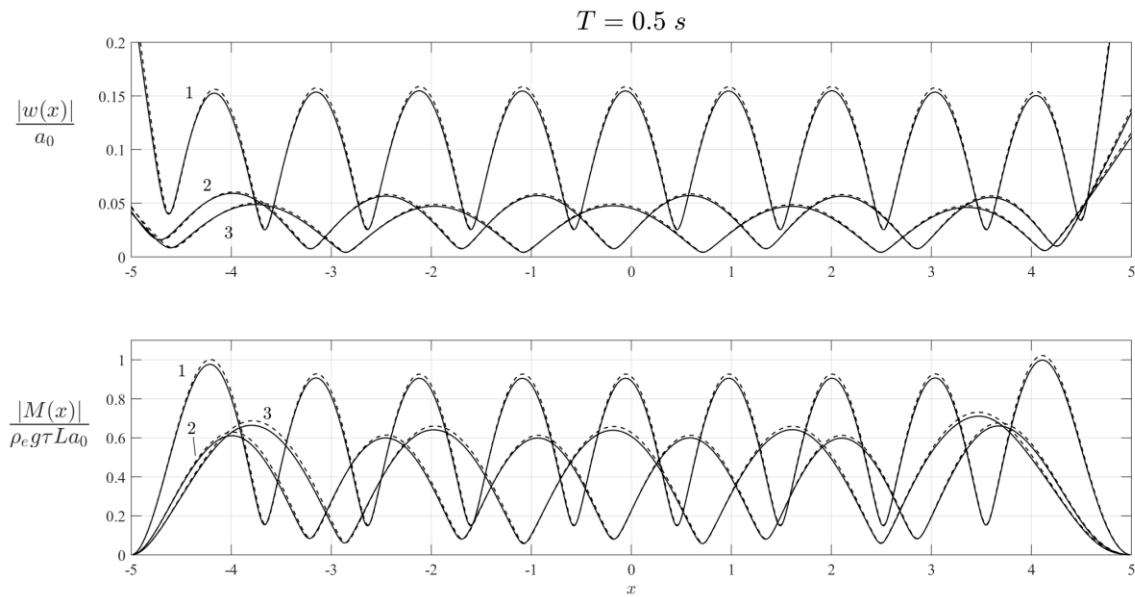
Fig. 11. Modulus of the non-dimensionalised deflection and moment for $T = 0.5\,s$ and different thickness values. Solid lines correspond to results obtained by the Kirchhoff plate model, while dashed line indicate results by Mindlin for thickness values (1) $\tau = 0.038\,\mathrm{m}$, (2) $\tau = 0.075\,\mathrm{m}$ and (3) $\tau = 0.1\,\mathrm{m}$.

(c)   Variable thickness case

Next, the reflection and transmission coefficients for a floating structure featuring thickness variation along its length are considered. A case considered in Smith and Meylan (2011) is examined. In the aforementioned analysis the results concern the hydroelastic response of a thin ice floe with length $L = 200\,m$ with set parameters $\rho = 900\,\text{kg}/\text{m}^3$, $v = 0.3$ and fluid density $\rho_w = 1000\,\text{kg}/\text{m}^3$. Concerning the employed Young's modulus the referenced work documents $E = 6\,\text{GPa}$, which corresponds to sea ice, however the provided details are insufficient. Following, Iida and Umazume (2020), that replicated the above case, an unrealistic Young's modulus $\tilde{E} = 6\,\text{TPa}$ is adopted for the structural modelling and deep water conditions are assumed. Two thickness profiles as in Smith and Meylan (2011) $\tau_i = d_0 q_i(x)$ are examined, employing the following distribution functions,

$$q_1(x) = 1 \text{ and } q_2(x) = 0.5 + 0.5\tanh(x - 0.5) + 0.5\tanh(1.5 - x),\ -100 < x < 100, \tag{50}$$

and a range of amplitudes d_0. The functions q_1 and q_2 of Eq. (50) correspond to a homogeneous thickness profile and a mollified step function distribution respectively, as seen in Fig. 12. The mean thickness values in τ_2 is equal to corresponding constant thickness τ_1 for varying d_0. The reflection coefficient versus a range of wave periods is plotted for four thickness amplitude values d_0 corresponding to thickness profiles τ_1 and τ_2. It is observed in Fig.12, that the results by the present method are found to be almost identical with Iida and Umazume (2020). The figure illustrates that qualitative differences between constant and variable thickness profiles become minor as d_0 increases, indicating that thickness variations are important for thin plates.

5.2.1   Thin plate floating over variable bathymetry

Next, the variable bathymetry effects are considered. Up to this point, constant seabed cases were considered for validation. In the sequel a series of comparisons with Belibassakis and Athanassoulis (2005), are carried out.
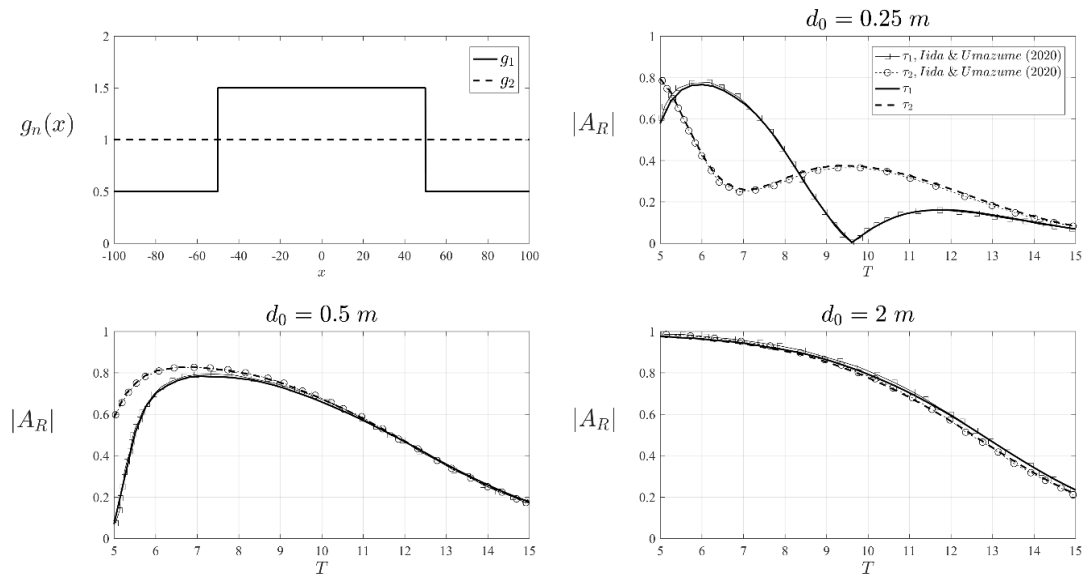
Fig. 12. Reflection coefficient vs period for thickness profiles τ_1, τ_2 and different values for d_0. The functions $g_n(x)$ are shown in the upper left subplot. The solid and dashed lines correspond to the solution

obtained by the present method for the two thickness profiles, while the square solid line and circle dashed line denote the corresponding results in Iida and Masuda 2020).

In the following cases, the responses of the floating plate considered in Section 5.2.1(a), are considered over different bathymetric profiles involving (a) a smooth shoaling (b) and undulating seabed.

(a) Smooth Shoal

Initially, a bathymetric profile representing a smooth shoal restricted in the hydroelastic region featuring the following depth function is considered,

$$h(x) = \frac{h_1 + h_2}{2} - \frac{h_1 - h_2}{2} \tanh\left(3\pi \left(\frac{x - a_1}{x - a_2} - \frac{1}{2} \right) \right) . \tag{51}$$

In Eq. (51), h_1 and h_2 are the constant depth values that correspond to subregions $\Omega^{(i)}$, $i = 1, 2$. An incident wave angular frequency is $\omega = 0.4$ rad s^{-1}. Two separate cases, with increasingly sloping bathymetry, are considered. The normalized response of a plate floating over a shoaling region with a slope of 3.8% corresponding to $h_1 = 12m$ and $h_2 = 8m$ in Eq. (51) and a shoal with a steeper slope 9.4% corresponding to $h_1 = 15m$ and $h_2 = 5m$ are given in Fig. 13. The solution by means of the present work is indicated by a solid line, while the results presented in Belibassakis and Athanassoulis (2005) are shown with squares. The two solutions are found in excellent agreement, noting the effectiveness of the method in variable bathymetry.
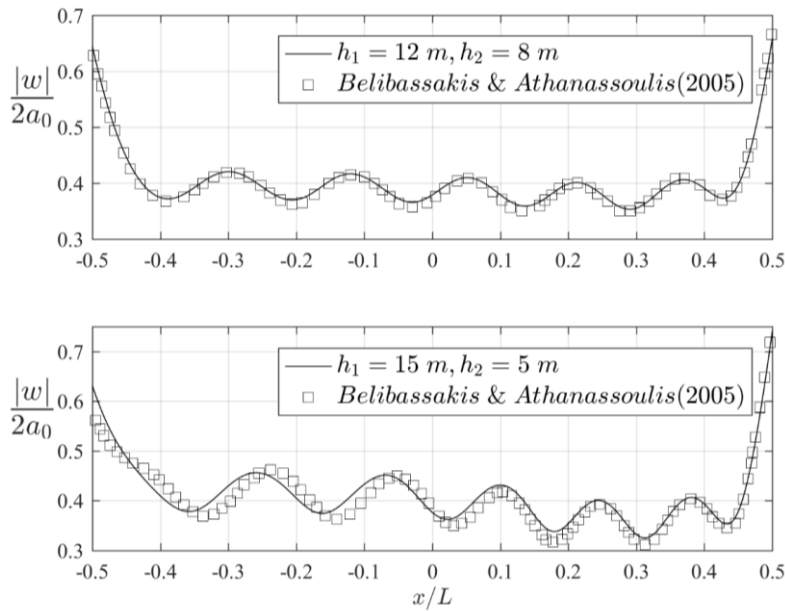
Fig. 13. Modulus of the normalised deflection to the waveheight for (top) $h_1 = 12$ m and $h_2 = 8$ m, (bottom) $h_1 = 15$ m and $h_2 = 5$ m.

(b) Undulating seabed

Next, the case of an undulating seabed is examined. The bathymetric profile is described by means of the following depth function,

$$h(x) = 10 - g(x) A_b \sin\left(k_b \left(x - a_1 \right) \right), \tag{52}$$

where $k_b = 2\pi/\lambda_b$ is the wavenumber of the seabed disturbance, $\lambda_b = 125m$ is the corresponding wavelength and A_b is the amplitude of undulations. The filtering function is given as,

$$g(x) = \left(1 - \exp\left(-\left(\frac{x - a_1}{\lambda_b}\right)^2\right)\right)\left(1 - \exp\left(-\left(\frac{x - a_2}{\lambda_b}\right)^2\right)\right). \tag{53}$$

The undulating profile is again restricted in the hydroelastic region, and disturbances are kept around a mean depth $h = 10m$. The incident wave field angular frequency is kept to $\omega = 0.4$ rad s^{-1}. In Fig. (14) the non-dimensional with respect to the wave height deflection corresponding to a variable seabed profile with $A_b/h = 15\%$ is plotted. The present method solution, drawn with a solid line compares favorably once again, with the results documented in Belibassakis and Athanassoulis (2005).
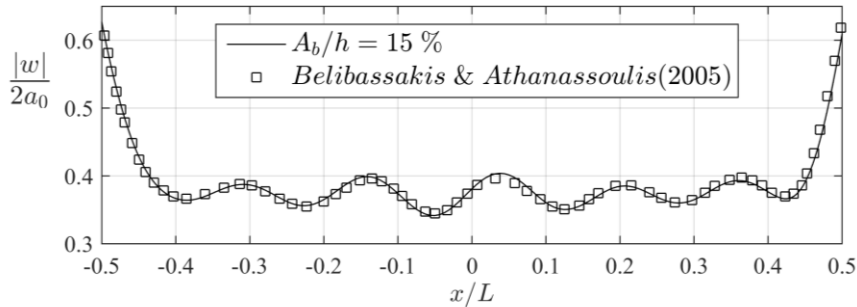
Fig. 14. Modulus of the normalised deflection to the waveheight for $A_b = 15\%$

6   Conclusions

The present contribution proposes a novel frequency domain method for the study of the hydroelastic interaction of small amplitude incident waves with inhomogeneous plates of negligible draft floating over 2D regions characterized by variable bathymetry. Field decomposition into diffraction and radiation components along with a modal expansion for the plate deflection, employing the *in vacuo* bending modes allows for the full decoupling of structural mechanics and hydrodynamic transformations. For the component hydrodynamic problems defined in the inhomogeneous strip, a weighted residuals approach in conjunction with a Lagrange multiplier formulation is followed to derive a weak problem involving the radiation-type potentials. Next, dimensionality reduction by means of the enhanced vertical representation for the wave potential, augmented by the sloping bottom mode, proposed by Athanassoulis and Belibassakis (1999) is performed. The FEM is employed for the treatment of the resulting 1D hydrodynamic weak problem, while the pressure condition on the plate-covered part of the fluid surface is imposed by means of Galerkin's method. Finally, the proposed method is validated against a series of numerical cases and experimental data documented in the literature and exhibited excellent performance.

A major advantage of the present contribution is that it carries no simplifying assumptions for the vertical structure of the wave-field or the bathymetric slope of the examined waveguide. The characteristics of the wave-field within the 2D region, as well as the bending moment and shear force distributions of the structure, can be recovered either straightforwardly or by trivial post-processing. Moreover, due to the treatment of the weak problem formulation, the C^2 smoothness requirement on the depth function, documented in Belibassakis and Athanassoulis (2005) is relaxed, enabling the treatment of more general profiles, while the numerical scheme remains rabidly convergent.

Regarding the structural modelling, the method is able to account for both material and geometric inhomogeneity, while first order shear effects and rotary inertia, relevant in high-frequency excitation scenarios, are also taken into account by means of the Mindlin plate model. Moreover, despite the augmented discretised system, the constrained formulation allows for the employment of conventional trial spaces, and the employment of classical FEM. A major advantage of the present method is its direct extensibility to treat the 3D problem, which is the subject of a future work, accounting for general bathymetry and structural shape. The aforementioned advantages will become even more pronounced as the method is expected to minimize the computational complexity of the full problem in an inhomogeneous setting. Finally, the method immediately allows for the structural modelling by means of higher-order plate theories with minimal reformulation.

Acknowledgements

Appendix A– Kirchhoff plate structural eigenvalue problem *in vacuo*

In the frequency domain, assuming a modal solution $W = \text{Re}\{w(x)\exp(-j\omega t)\}$ the eigenvalue problem of an unconstrained thin plate, under cylindrical bending assumptions is given by,

$$\partial_{xx}\left(D(x)\partial_{xx}w(x)\right) - \omega^2 \rho_e \tau(x) w(x) = 0. \tag{A1}$$

Introducing the weight function $v \in H^2$ the weak form of problem (A1) is retrieved ,

$$\int_{-L/2}^{L/2} \partial_{xx}v\left(D(x)\partial_{xx}w(x)\right)dx - \omega^2 \int_{-L/2}^{L/2} \rho_e\tau(x)w(x)v\,dx + \left[v\,D(x)\partial_{xx}w(x)\right]_{-L/2}^{L/2}$$
$$- \left[\partial_x v \partial_x\left(D(x)\partial_{xx}w(x)\right)\right]_{-L/2}^{L/2} = 0. \tag{A2}$$

In the unconstrained case the boundary terms vanish due to the zero moment and zero shear force boundary conditions at the plate edges. In order to satisfy the conformity condition, unknown $w(x)$ is interpolated using Hermite (C^1) shape functions as,

$$w(x) = \sum_{i}^{N} H_i(x)w_i, \tag{A3}$$

where N is the number of nodes in the 1-D elements. Assuming a discretization with Hermite elements of *N+1* order and arranging the elemental unknowns $\mathbf{u}_e = \begin{bmatrix} w_1 & \partial_x w_1 & \cdots & w_N & \partial_x w_N \end{bmatrix}^T$ the interpolation of the unknowns are written as,

$$w = \begin{bmatrix} H_1 & H_2 & \cdots & H_{2N-1} & H_{2N} \end{bmatrix} u_e = \mathbf{L}\,\mathbf{u_e}, \tag{A4}$$

Substituting (A4) in (A2) and allowing the weight functions to reduce to the hermite shape functions results in the element matrices,

$$kloc = \int_{x_e} \mathbf{L}^T D(x)\mathbf{L}\,dx \text{ and } mloc = \int_{x_e} \mathbf{L}^T \rho_e\tau(x)\mathbf{L}\,dx \ . \tag{A5}$$

Finally, upon assembly the discretized system it terms of the global uknowns is written as,

$$\mathbf{K}\,\mathbf{u}\ =-\omega^{2}\mathbf{M}\,\mathbf{u}\quad. \tag{A6}$$

Appendix B–Mindlin plate structural eigenvalue problem *in vacuo*

In the frequency domain the eigenvalue problem of a free moderately thick plate (1st order shear deformation effects), under cylindrical bending assumptions is given by the following system with length L spanning over $-L/2 < x < L/2$,

$$-\omega^{2}\rho_{e}\tau w-\partial_{x}\left(\kappa G\tau\left(\partial_{x}w-\theta\right)\right)=0 \quad, \tag{B1a}$$

$$-\omega^{2}I_{r}\theta-\kappa G\tau\left(\partial_{x}w-\theta\right)-\partial_{x}\left[D\partial_{x}\theta\right]=0, \tag{B1b}$$

involving the unknown deflection $w(x)$, $\theta(x)$ and rotation.

Multiplying by the weight functions v_{1}, $v_{2} \in H^{1}$ and integrating over the plate length and performing integration by parts yields,

$$-\omega^{2}\int_{-L/2}^{L/2}v_{1}\rho_{e}\tau w\,dx+\int_{-L/2}^{L/2}\partial_{x}v_{1}\left(\kappa G\tau\left(\partial_{x}w-\theta\right)\right)dx-\left[v_{1}\kappa G\tau\left(\partial_{x}w-\theta\right)\right]_{-L/2}^{L/2}=0 \quad, \tag{B2a}$$

$$-\omega^{2}\int_{-L/2}^{L/2}v_{1}I_{r}\theta\,dx-\int_{-L/2}^{L/2}v_{2}\kappa G\tau\left(\partial_{x}w-\theta\right)dx+\int_{-L/2}^{L/2}\partial_{x}v_{2}D\partial_{x}\theta\,dx-\left[v_{2}D\partial_{x}\theta\right]_{-L/2}^{L/2}=0. \tag{B2b}$$

For the unconstrained case, the zero force and zero moment conditions cause the boundary terms to vanish in Eqs. (B2). Next, the unknowns w , θ are interpolated using Lagrange (C^{0}) shape functions as,

$$w(x)=\sum_{i}^{N}N_{i}(x)w_{i},\ \theta(x)=\sum_{i}^{N}N_{i}(x)\theta_{i} \tag{B3}$$

where N is the number of nodes in the 1-D elements.

Assuming a discretization with Lagrange elements of *N-1* order and arranging the elemental unknowns $\mathbf{u}_{e}=\begin{bmatrix}w_{1} & \theta_{1} & \cdots & w_{N} & \theta_{N}\end{bmatrix}^{T}$ the interpolation of the unknowns are written as,

$$w=\begin{bmatrix}N_{1} & 0 & N_{2} & \cdots & N_{N} & 0\end{bmatrix}\mathbf{u_{e}}=\mathbf{L_{1}u_{e}},\ \theta=\begin{bmatrix}0 & N_{1} & 0 & \cdots & 0 & N_{N}\end{bmatrix}\mathbf{u_{e}}=\mathbf{L_{2}u_{e}}. \tag{B4}$$

The element mass matrices for the discrete form of equations of system of Eqs. (B2) read,

$$\mathrm{mloc}=\int_{x_{e}}\mathbf{L_{1}}^{T}\rho_{e}\tau\mathbf{L_{1}}\ dx+\int_{x_{e}}\mathbf{L_{2}}^{T}I_{r}\mathbf{L_{2}}\ dx \tag{B5a}$$

while the stiffness matrices for Eq.,

$$\mathrm{kloc}\ =\int_{x_{e}}\partial_{x}\mathbf{L_{1}}^{T}\kappa G\tau\partial_{x}\mathbf{L_{1}}\ dx\ +\int_{x_{e}}\partial_{x}\mathbf{L_{1}}^{T}\kappa G\tau\mathbf{L_{2}}$$
$$+\int_{x_{e}}\mathbf{L_{2}}^{T}\kappa G\tau\partial_{x}\mathbf{L_{1}}dx+\int_{x_{e}}\mathbf{L_{2}}^{T}\kappa G\tau\mathbf{L_{2}}dx+\int_{x_{e}}\partial_{x}\mathbf{L_{2}}^{T}D\partial_{x}\mathbf{L_{2}}\ dx \tag{B5b}$$

By means of Eqs. (B5a,b) and after assembly the discretized system it terms of the global unknowns is written as

$$\mathbf{K}\,\mathbf{u} \ = -\omega^{2}\mathbf{M}\,\mathbf{u} \ . \tag{B6}$$

The following table summarizes comparisons of the above brute force approach for the treatment of the structural eigenvalue problem, employing 5th order Lagrange interpolations against results published in Shi et al. (2015).

Table B1 Non-dimensional frequency for the free-free plate with κ=5/6 and ν=0.3

	$\tau/L=0.02$			$\tau/L=0.05$		
	Present method	Shi et al. (2015).	Deviation (%)	Present method	Shi et al. (2015).	Deviation (%)
1	4.7264	4.7266	3.44365E-05	4.7266	4.7266	0.000228567
2	7.8359	7.8369	0.000131751	7.8369	7.8369	0.000686446
3	10.9481	10.951	0.000266486	10.951	10.951	0.001380529
4	14.0366	14.043	0.000451865	14.043	14.043	0.002267211
5	17.0968	17.109	0.000712542	17.109	17.109	0.003218165
6	23.1119	20.144	0.147333982	20.144	20.144	0.004194369
	$\tau/L=0.1$			$\tau/L=0.2$		
1	4.6452	4.6489	0.000797372	4.4399	4.4509	0.00248027
2	7.4797	7.4996	0.002648226	6.7619	6.8082	0.006805071
3	10.0829	10.131	0.004752404	8.6930	8.7839	0.010346259
4	12.4312	12.518	0.006934663	10.2852	10.426	0.013500627
5	14.5526	14.684	0.008946874	11.6263	11.817	0.016134918
6	16.4781	16.657	0.010740499	12.5723	12.850	0.021611999

References

Athanassoulis, G.A., Belibassakis, K.A., 1999. A consistent coupled-mode theory for the propagation of small-amplitude water waves over variable bathymetry regions. J. Fluid Mech. 389, 275–301. https://doi.org/10.1017/S0022112099004978

Athanassoulis, M.A., Belibassakis, K., 2009. A novel coupled-mode theory with application to hydroelastic analysis of thick, non-uniform floating bodies over general bathymetry. Proc. Inst. Mech. Eng. Part M J. Eng. Marit. Environ. 223, 419–438. https://doi.org/10.1243/14750902JEME150

Belibassakis, K.A., 2008. A boundary element method for the hydrodynamic analysis of floating bodies in variable bathymetry regions. https://doi.org/10.1016/j.enganabound.2008.02.003

Belibassakis, K.A., Athanassoulis, G.A., 2005. A coupled-mode model for the hydroelastic analysis of large floating bodies over variable bathymetry regions. J. Fluid Mech. 531, 221–249. https://doi.org/10.1017/S0022112005004003

Bennetts, L.G., Biggs, N.R.T., Porter, D., 2007. A multi-mode approximation to wave scattering by ice sheets of varying thickness. J. Fluid Mech. 579, 413–443. https://doi.org/10.1017/S002211200700537X

Benzi, M., Golubt, G.H., Liesen, J., 2005. Numerical solution of saddle point problems. Acta Numer. 14, 1–

137. https://doi.org/10.1017/S0962492904000212

Bishop, R.E.D., Price, W.G., 1976. On the relationship between "dry modes" and "wet modes" in the theory of ship response. J. Sound Vib. https://doi.org/10.1016/0022-460X(76)90595-2

Brezzi, F., Fortin, M., 1991. Mixed and Hybrid Finite Element Methods, Springer. https://doi.org/10.1007/978-1-4612-3172-1

Faltinsen, O.M., 2015. Hydrodynamics of marine and offshore structures. J. Hydrodyn. https://doi.org/10.1016/S1001-6058(14)60092-5

Finlayson, B.A., 2013. The Method of Weighted Residuals and Variational Principles. Method Weight. Residuals Var. Princ. https://doi.org/10.1137/1.9781611973242

Fox, C., Squire, V.A., 1991. Coupling between the ocean and an ice shelf. Ann. Glaciol. 15, 101–108. https://doi.org/10.3189/1991aog15-1-101-108

Gerostathis, T.P., Belibassakis, K.A., Athanassoulis, G.A., 2016. 3D hydroelastic analysis of very large floating bodies over variable bathymetry regions. J. Ocean Eng. Mar. Energy 2, 159–175. https://doi.org/10.1007/s40722-016-0046-6

Hazard, C., Lunéville, E., 2008. An improved multimodal approach for non-uniform acoustic waveguides. IMA J. Appl. Math. (Institute Math. Its Appl. 73, 668–690. https://doi.org/10.1093/imamat/hxn006

Hermans, A.J., 2003. The ray method for the deflection of a floating flexible platform in short waves. J. Fluids Struct. 17, 593–602. https://doi.org/10.1016/S0889-9746(02)00148-2

Hughes, T.J.R., 2000. The Finite Element Method: Linear Static and Dynamic Finite ELement Analysis, Dover Publications.

Iida, T., Umazume, K., 2020. Wave response of segmented floating plate and validation of its homogenized solution. Appl. Ocean Res. 97, 102083. https://doi.org/10.1016/j.apor.2020.102083

Ilyas, M., Meylan, M.H., Lamichhane, B., Bennetts, L.G., 2018. Time-domain and modal response of ice shelves to wave forcing using the finite element method. J. Fluids Struct. https://doi.org/10.1016/j.jfluidstructs.2018.03.010

Kantorovich, L. V., Krylov, V.I., 1960. Approximate Methods of Higher Analysis, 4th ed. ed. Interscience Pub., New York.

Karperaki, A.E., Belibassakis, K.A., Papathanasiou, T.K., 2016. Time-domain, shallow-water hydroelastic analysis of VLFS elastically connected to the seabed. Mar. Struct. 48. https://doi.org/10.1016/j.marstruc.2016.04.002

Kashiwagi, M., 1998. A B-spline Galerkin scheme for calculating the hydroelastic response of a very large floating structure in waves. J. Mar. Sci. Technol. 3, 37–49. https://doi.org/10.1007/BF01239805

Kyoung, J.H., Hong, S.Y., Kim, B.W., Cho, S.K., 2005. Hydroelastic response of a very large floating structure over a variable bottom topography. Ocean Eng. 32, 2040–2052. https://doi.org/10.1016/j.oceaneng.2005.03.003

Linton, C.M., McIver, P., 2001. Handbook of mathematical techniques for wave/structure interactions. Handb. Math. Tech. Wave/Structure Interact. https://doi.org/10.1201/9781420036060

Liu, X., Wang, X., Xu, S., 2020. A DMM-EMM-RSM hybrid technique on two-dimensional frequency-domain hydroelasticity of floating structures over variable bathymetry. Ocean Eng. 201, 107135. https://doi.org/10.1016/j.oceaneng.2020.107135

Magoulès, F., Roux, F.X., 2006. Lagrangian formulation of domain decomposition methods: A unified theory. Appl. Math. Model. 30, 593–615. https://doi.org/10.1016/j.apm.2005.06.016

Massel, S.R., 1993. Extended refraction-diffraction equation for surface waves. Coast. Eng. 19, 97–126. https://doi.org/10.1016/0378-3839(93)90020-9

Newman, J.N., 1994. Wave effects on deformable bodies. Appl. Ocean Res. https://doi.org/10.1016/0141-1187(94)90013-2

Nguyen, H.P., Wang, C.M., Flocard, F., Pedroso, D.M., 2019. Extracting energy while reducing hydroelastic responses of VLFS using a modular raft wec-type attachment. Appl. Ocean Res. 84, 302–316. https://doi.org/10.1016/j.apor.2018.11.016

Papathanasiou, T.K., Belibassakis, K.A., 2018. Resonances of enclosed shallow water basins with slender floating elastic bodies. J. Fluids Struct. 82, 538–558. https://doi.org/10.1016/j.jfluidstructs.2018.08.006

Papathanasiou, T.K., Karperaki, A., Theotokoglou, E.E., Belibassakis, K.A., 2015. A higher order FEM for time-domain hydroelastic analysis of large floating bodies in an inhomogeneous shallow water environment. Proc. R. Soc. A Math. Phys. Eng. Sci. 471. https://doi.org/10.1098/rspa.2014.0643

Papathanasiou, T.K., Karperaki, A.E., Belibassakis, K.A., 2019. On the resonant hydroelastic behaviour of ice shelves. Ocean Model. 133, 11–26. https://doi.org/10.1016/j.ocemod.2018.10.008

Porter, D., Porter, R., 2004. Approximations to wave scattering by an ice sheet of variable thickness over undulating bed topography. J. Fluid Mech. 509, 145–179. https://doi.org/10.1017/S0022112004009267

Porter, D., Staziker, D.J., 1995. Extensions of the Mild-Slope Equation. J. Fluid Mech. 300, 367–382. https://doi.org/10.1017/S0022112095003727

Porter, R., 2019. The coupling between ocean waves and rectangular ice sheets. J. Fluids Struct. https://doi.org/10.1016/j.jfluidstructs.2018.09.004

Porter, R., Porter, D., 2000. Water wave scattering by a step of arbitrary profile. J. Fluid Mech. 411, 131–164. https://doi.org/10.1017/S0022112099008101

Praveen, K.M., Karmakar, & D., Soares, & C.G., Karmakar, D., Soares, C.G., 2019. Influence of Support Conditions on the Hydroelastic Behaviour of Floating Thick Elastic Plate. J. Mar. Sci. Appl. https://doi.org/10.1007/s11804-019-00104-7

Praveen, K.M., Karmakar, D., 2019. Wave transformation due to floating elastic thick plate over changing bottom topography, in: Lecture Notes in Civil Engineering. Springer, pp. 417–430. https://doi.org/10.1007/978-981-13-3134-3_31

Shi, D., Wang, Q., Shi, X., Pang, F., 2015. An accurate solution method for the vibration analysis of Timoshenko beams with general elastic supports. Proc. Inst. Mech. Eng. Part C J. Mech. Eng. Sci. 229, 2327–2340. https://doi.org/10.1177/0954406214558675

Smith, M.J.A., Meylan, M.H., 2011. Wave scattering by an ice floe of variable thickness. Cold Reg. Sci. Technol. https://doi.org/10.1016/j.coldregions.2011.03.003

Squire, V.A., 2008. Synergies between VLFS hydroelasticity and sea-ice research. Proc. Int. Offshore Polar Eng. Conf. 8, 1–13.

Stoker, J.J., 1967. Water Waves, Water Waves: The Mathematical Theory with Application. John Wiley & Sons, Inc., Hoboken, NJ, USA. https://doi.org/10.1002/9781118033159

Takagi, K., Shimada, K., Ikebuchi, T., 2000. Anti-motion device for a very large floating structure. Mar. Struct. 13, 421–436. https://doi.org/10.1016/S0951-8339(00)00018-6

Taylor, R.E., Waite, J.B., 1978. The dynamics of offshore structures evaluated by boundary integral techniques. Int. J. Numer. Methods Eng. 13, 73–92. https://doi.org/10.1002/nme.1620130106

Utsunomiya, T., Watanabe, E., Wu, C., Hayashi, N., Nakai, K., Sekita, K., 1995. Wave response analysis of a flexible floating structure by be-fe combination method, in: Proceedings of the International Offshore and Polar Engineering Conference. International Society of Offshore and Polar Engineers, pp. 400–405.

Wang, C.M., Watanabe, E., Utsunomiya, T., 2006. Very large floating structures, London: CRC Press. https://doi.org/10.1201/9781482265927

Watanabe, E., Utsunomiya, T., Wang, C.M., 2004. Hydroelastic analysis of pontoon-type VLFS: A literature survey. Eng. Struct. https://doi.org/10.1016/j.engstruct.2003.10.001

Wu, C., Watanabe, E., Utsunomiya, T., 1995. An eigenfunction expansion-matching method for analyzing the wave-induced responses of an elastic floating plate. Appl. Ocean Res. https://doi.org/10.1016/0141-1187(95)00023-2

Zhao, C., Hu, C., Wei, Y., Zhang, J., Huang, W., 2008. Diffraction of surface waves by floating elastic plates. J. Fluids Struct. 24, 231–249. https://doi.org/10.1016/j.jfluidstructs.2007.07.006

Zienkiewicz, O., Taylor, R., 2005. The finite element method, 6th ed.